On the importance of modeling fMRI transients when estimating effective connectivity

Document status and date:
Published: 01/07/2017

DOI:
10.1016/j.neuroimage.2017.03.017

Document Version:
Publisher's PDF, also known as Version of record

Document license:
Taverne

Please check the document version of this publication:

• A submitted manuscript is the version of the article upon submission and before peer-review. There can be important differences between the submitted version and the official published version of record. People interested in the research are advised to contact the author for the final version of the publication, or visit the DOI to the publisher's website.
• The final author version and the galley proof are versions of the publication after peer review.
• The final published version features the final layout of the paper including the volume, issue and page numbers.

Link to publication

Download date: 28 Apr. 2024

CrossMark

On the importance of modeling fMRI transients when estimating effective connectivity: A dynamic causal modeling study using ASL data

Martin Havlicek[a],[*],[1], Alard Roebroeck[a], Karl J. Friston[b], Anna Gardumi[a], Dimo Ivanov[a], Kamil Uludag[a],[1]

[a] Department of Cognitive Neuroscience, Faculty of Psychology and Neuroscience, Maastricht University, 6200MD Maastricht, The Netherlands
[b] Wellcome Trust Centre for Neuroimaging, Institute of Neurology, University College London, London WC1N 3BG, United Kingdom

ARTICLE INFO

ABSTRACT

Effective connectivity is commonly assessed using blood oxygenation level-dependent (BOLD) signals. In (Havlicek et al., 2015), we presented a novel, physiologically informed dynamic causal model (P-DCM) that extends current generative models. We demonstrated the improvements afforded by P-DCM in terms of the ability to model commonly observed neuronal and vascular transients in single regions. Here, we assess the ability of the novel and previous DCM variants to estimate effective connectivity among a network of five ROIs driven by a visuo-motor task. We demonstrate that connectivity estimates depend sensitively on the DCM used, due to differences in the modeling of hemodynamic response transients; such as the post-stimulus undershoot or adaptation during stimulation. In addition, using a novel DCM for arterial spin labeling (ASL) fMRI that measures BOLD and CBF signals simultaneously, we confirmed our findings (by using the BOLD data alone and in conjunction with CBF). We show that P-DCM provides better estimates of effective connectivity, regardless of whether it is applied to BOLD data alone or to ASL time-series, and that all new aspects of P-DCM (i.e. neuronal, neurovascular, hemodynamic components) constitute an improvement compared to those in the previous DCM variants. In summary, (i) accurate modeling of fMRI response transients is crucial to obtain valid effective connectivity estimates and (ii) any additional hemodynamic data, such as provided by ASL, increases the ability to disambiguate neuronal and vascular effects present in the BOLD signal.

Introduction

Functional neuroimaging is widely used to investigate functional integration in the human brain (Friston, 2011), which is commonly characterized by functional or effective connectivity (Friston, 1994). While functional connectivity describes statistical dependencies among brain activations at the level of observed data, effective connectivity is defined as causal influence that (inferred) neuronal systems exert over another. Thus, determining effective connectivity requires a physically and physiologically motivated (causal) model linking local activation and distributed interactions among neuronal responses to the measured data. The requisite generative models have been proposed for several noninvasive neuroimaging modalities, such as functional magnetic resonance imaging (fMRI) (Friston et al., 2003) and electro- and magneto- encephalography (EEG and MEG) (David et al., 2006; Valdes Sosa et al., 2009) or functional near-infrared spectroscopy (fNIRS) (Tak et al., 2015).

A prominent modeling framework for estimating effective connectivity from BOLD data is dynamic causal modeling (DCM) (Friston et al., 2003). DCM has been extensively used both in healthy subjects and patient studies (see e.g. review by Seghier (2010) and references therein). The generative model of DCM for fMRI data comprises: (i) a neuronal model, in which neuronal activity in one region causes changes in its own activity (via *intrinsic* connections) and neuronal activity in distal regions (via long-range *extrinsic* connections); (ii) a model of neurovascular coupling (NVC) that links region-specific neuronal activity to local changes in cerebral blood flow (CBF); (iii) a hemodynamic model that transforms blood inflow to changes in cerebral blood volume (CBV) and blood oxygenation; and finally (iv) a physical model translating these changes into the measured BOLD signal.

To estimate effective connectivity from fMRI data using DCM, testable hypotheses about how brain areas are connected and how they change with tasks are required. These hypotheses entail assumptions

---

about the connectivity architecture, and how it is affected by experimental manipulations (Stephan et al., 2010). Then, using Bayesian inference, DCM fits the BOLD data by tuning the connectivity and hemodynamic parameters so that the discrepancy between modeled and observed fMRI time-courses is minimized under complexity constraints (Penny et al., 2010). This means that the aim of DCM is not only to provide accurate fits to observed data, but also to account for the model complexity, such that more complex models are automatically penalized. The ensuing Bayesian approach enables one not only to estimate model parameters, but also to compare different models in terms of their evidence; i.e. accuracy minus complexity (Penny et al., 2010).

Although Bayesian model selection (BMS) is typically used to choose between different neuronal architectures, it can also be used to identify the most likely physiological or physical mechanism underlying any component of the generative model ((i-iv) above). Examples of this sort of Bayesian model comparison can be found in Stephan et al. (2008, 2007), who compared linear vs. nonlinear neuronal connectivity models and several forms of BOLD generation equations. Furthermore, Marreiros et al. (2008) compared single-state vs. two-state neuronal models, while Rosa et al. (2011) compared different types of electro-physiological models of NVC, using simultaneous EEG and fMRI recordings.

Recently, we introduced a physiologically informed generative model for BOLD DCM (Havlicek et al., 2015), called P-DCM, which extended and updated the standard model used in DCM for fMRI (S-DCM) (Friston et al., 2003) and two-state extension (2S-DCM) (Marreiros et al., 2008) in four key aspects (see also Fig. 1):

1. At the neuronal level, we model local neuronal activity as interacting excitatory and inhibitory (E-I) neuronal populations, allowing fine-tuning of adaptive responses during stimulation and post-stimulation periods – of the sort seen in electrophysiological data. Different brain areas are effectively connected via positive and negative long-range extrinsic connections among excitatory populations.
2. The neurovascular coupling (NVC) – CBF changes evoked by changes in neuronal activity – is strictly feedforward. That is, CBF

represents a smoothed version of the neuronal activity.

3. In the hemodynamic model, CBV can be uncoupled from CBF during transient periods due to viscoelastic properties of the post-capillary blood compartments (as in the original balloon model (Buxton et al., 1998)).
4. Finally, sequence-specific parameters of the BOLD signal equation were provided for both GE and SE MRI sequences and for different magnetic field strengths.

In our previous paper (Havlicek et al., 2015), we demonstrated that these extensions allow for a more accurate modeling of single-ROI BOLD responses compared to S-DCM and 2S-DCM, while simultaneously providing higher statistical evidence. This was, in particular, due to the more accurate characterization of the neuronal and vascular origins of the BOLD signal transients; such as response adaptation and post-stimulus undershoot. In the current paper, we evaluate the consequences of model differences when modeling effective connectivity between regions.

The separation of neuronal from hemodynamic parameters in any variant of DCM can be confounded by the fact that the BOLD signal results from a complex interplay between region-specific CBF, CBV and cerebral metabolic rate of oxygen metabolism (CMRO$_2$). That is, even for the same neuronal activity, the BOLD signal time-course can vary between different subjects, brain areas and even voxels in the same brain area due to differences in NVC and CBF-CBV coupling (e.g. see Handwerker et al. (2004), Renvall et al. (2014)). This means that vascular transients can mask or distort neuronal transients. Therefore, any additional experimental data that allows disentangling neuronal and ensuing vascular transients has the potential to increase the validity of the connectivity estimates offered by DCM.

In principle, DCM can also be applied to other fMRI acquisition modalities, such as arterial spin labeling (ASL) (Liu and Brown, 2007), which additionally measures cerebral blood flow (CBF), or vascular occupancy (VASO) (Huber et al., 2014; Lu et al., 2003), which measures cerebral blood volume (CBV). In fact, when considering the causal chain of physiological processes that follows neuronal activation, CBF and CBV signals are more closely related to the neuronal signal
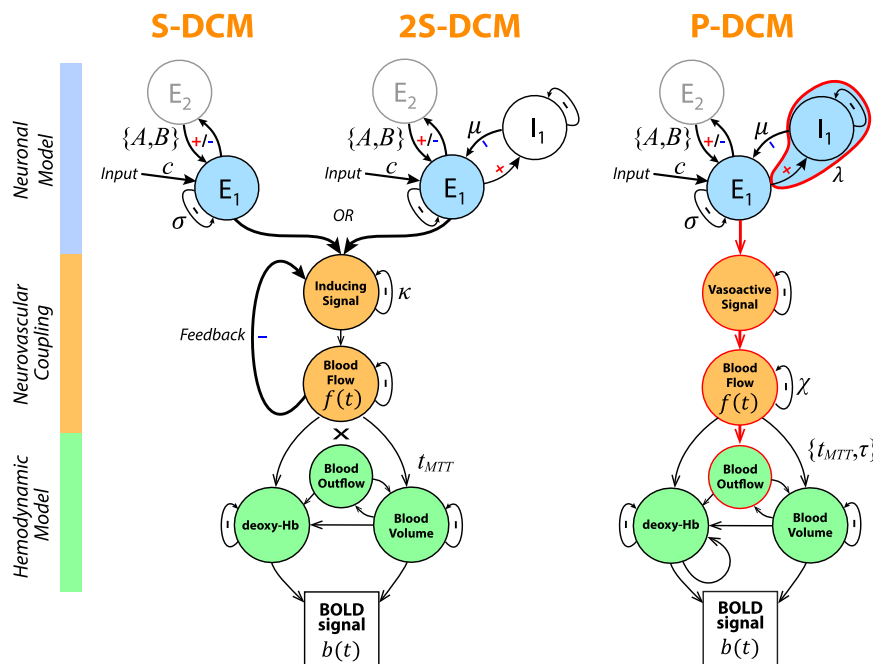
Fig. 1. Scheme illustrating the organization of generative models entailed by S-DCM, 2S-DCM and P-DCM. Three main parts of the generative models; i.e. neuronal model, neurovascular coupling and hemodynamic model, are colored in blue, orange and green, respectively. Main differences in P-DCM with respect to S- and 2S-DCM (see Havlicek (2015)) are highlighted with red color, such as the adaptive part of the two state-neuronal model, feedforward NVC and CBF-CBV uncoupling modeled in the blood outflow. The parameters that are associated with optimization of specific model components during DCM analyses are displayed.

compared to the BOLD signal. In the current paper, we further extend the DCM for BOLD fMRI, described above, to model ASL signals; where we jointly model both CBF and BOLD responses to stimulus-induced neuronal activations. By using ASL data, we hope to disambiguate between neuronal and vascular mechanisms contributing to the BOLD signals more efficiently, and thus improve the reliability of connectivity estimates. Since ASL simultaneously acquires BOLD signal and CBF, it affords the unique opportunity to compare connectivity estimates as a function of the fMRI data used (BOLD signal alone or BOLD signal together with CBF) and to evaluate the impact of physiological mechanisms entailed by different DCM variants (S-, 2S and P-DCM) on connectivity estimates.

In summary, the primary aim of this paper is to compare P-DCM with S- and 2S-DCM when applied to a network of brain regions activated by a visuo-motor task. In particular, we assess the impact of modeling response transients on effective connectivity estimates. Crucially, the implicit model comparison and identification is performed using BOLD data alone and ASL data. This enable us to establish the validity of effective connectivity estimates based on BOLD data alone (as it is typically applied in DCM studies); relative to the equivalent estimates that are informed by concurrent CBF measurements.

Materials and methods

Experimental data

Data acquisition and experimental task

MR images were acquired on 3T Siemens Prisma scanner (Siemens Medical Solutions, Erlangen, Germany) from five healthy subjects (right-handed females; age range: 24–31). The subjects gave informed consent prior to scanning, according to the guidelines of the local ethics committee of the Faculty of Psychology & Neuroscience, Maastricht University. Following a localizer scan, MPRAGE T1-weighted anatomical images with 1 mm isotropic voxel size were acquired. Functional CBF and BOLD signals were measured using a PICORE-Q2TIPS ASL (Wong et al., 1997) sequence with the following parameters: TR=2200 ms; TE=17 ms; flip-angle=80°; FOV=256×256 mm^2; voxel size=3×3×3 mm^3; TI1=900 ms; TI2=1600 ms. Ten oblique slices covering early visual and motor areas were acquired in descending order. A descending order of slice acquisition was chosen to acquire the motor cortex first, which is known to have slightly shorter arterial arrival time (~800 ms) compared to the visual cortex (~900 ms) (Donahue et al., 2014). The tag was 10 cm in width positioned at a 1 cm gap inferior to the imaging slices.

Each subject performed 4 runs (each 382 TRs long) of a visuo-motor task consisting of 4 conditions arranged in blocks interspersed with resting fixation baseline periods (see Fig. 3A). During the entire experiment, subjects fixated a white cross in the middle of the projected screen. The grey background was isoluminant with a 150° checkerboard wedge (black and white) stimulus presented either on the left or right visual field. During the two ipsilateral conditions (either left or right), subjects were instructed to respond to the visual stimulation (appearing for 200 ms) with sequential ipsilateral finger tapping (thumb-index, thumb-middle and thumb-index finger). During the two contralateral conditions (either left or right), subjects were instructed to respond to visual stimulation with the contralateral hand. Ipsilateral and contralateral conditions were indicated by a color change of the white fixation cross – blue for the ipsilateral conditions and red for the contralateral conditions. During the resting periods, subjects were instructed to continue fixating on the white cross. Visual stimuli for each condition were organized into 14 s blocks (each included 11 events with randomized ISI lasting at least 1 s) followed by 26 s resting period. The initial and final rest conditions were 37 and 38 s in duration, respectively. Blocks of ipsilateral and contralateral con-

ditions (20 blocks in each run) were pseudo-randomized within and between runs.

Preprocessing and ROI selection

The data were preprocessed using SPM12 (R6470) package (http://www.fil.ion.ucl.ac.uk/spm). Functional data from each subject were realigned to the first volume of the first run to correct for head motion. This was performed separately for control and tagged images obtained with the ASL sequence. The mean tagged image was then coregistered to the mean control image and the transformation matrix was applied to all the tagged images. The mean of the realigned functional time-series was coregistered to the anatomical image and the latter was used to segment gray matter, white matter and CSF. The spatial transformation parameters from the segmentation were used to spatially normalize the anatomical and functional images into MNI space, and the latter were further smoothed with a 4 mm FWHM isotropic Gaussian kernel.

To localize the brain regions responding to the experimental manipulations, the ASL data were modeled voxel-wise using a general linear model (GLM) that included the tasks (two ipsilateral and two contralateral conditions) in all four runs. In particular, a GLM of the ASL signal was constructed to reflect the simultaneous contributions of CBF and BOLD signal changes (see Fig. 2A, for details on this ASL model see (Mumford et al., 2006)):

$$y = \beta_0 + x_{CBF_0} \cdot \beta_1 + x_{BOLD} \cdot \beta_2 + x_{CBF_0} \cdot x_{BOLD} \cdot \beta_3 + H_0 \cdot \gamma_{1:K} + \varepsilon, \tag{1}$$

where y is a vector that contains the voxels' time-courses. Besides the standard intercept, β_0, representing the baseline of static MR signal, we included a task-independent explanatory variable, x_{CBF_0}, representing baseline CBF that simulates the alternation of tagged and control signals ($x_{CBF_0}(t)=(-1)^t$; i.e. -1 associated with tagged time points and $+1$ with control time points). The parameter β_1 is then proportional to the tag and control MRI signal magnitude difference and, hence, is proportional to the amount of tagged blood delivered to the local tissue. Each task condition was modeled with two explanatory variables: The first predictor represents the BOLD response (x_{BOLD}) generated by a convolution of the stimulus function with a double-gamma hemodynamic response function. As in previous studies (Hernandez-Garcia et al., 2010; Mumford et al., 2006), the second predictor represents the CBF response that was approximated using the same BOLD response model (x_{BOLD}) but modulated by CBF baseline (x_{CBF_0}); i.e. yielding an interaction term $x_{CBF_0} \cdot x_{BOLD}$. The parameters β_2 and β_3 are therefore proportional to the relative contributions of BOLD and CBF responses to the ASL signal[2]. Additionally, low-frequency signal drifts (with cutoff period of 180 s) were modeled in matrix H_0 using discrete cosine transform basis functions. The error vector $\varepsilon = \mathcal{N}(0, \sigma^2 V)$ models colored noise using a first-order autoregressive model with intrinsic autocorrelation matrix V. This GLM was estimated using standard estimation routines in SPM12 software. Contrast images were created for each condition, assuming ('global') conjunction of CBF and BOLD model estimates (Friston et al., 2005). The statistical threshold was set at $p < 0.05$, corrected for family-wise errors (FWE).

Finally, five regions of interests (ROIs) were defined from significant responses to the visuo-motor task in both CBF and BOLD signals. In particular, ROIs centered in left and right V1, left and right M1 and SMA were selected. Voxel contributions from left and right SMA were considered together as their time-courses looked almost identical. Additionally, regions labeled as V1 and M1 most likely include partial contributions from V2 and S1 and PMC, respectively. The ASL signals (corrected for the low frequency fluctuations; cut-off=1/180 s) were

---

[2] Note that we initially also included second and third temporal derivatives of the hemodynamic response to account for variability in response shape between brain areas in both CBF and BOLD signal component. However, we did not observe any significant differences in activation locations; therefore, we only report the results using the basic model.
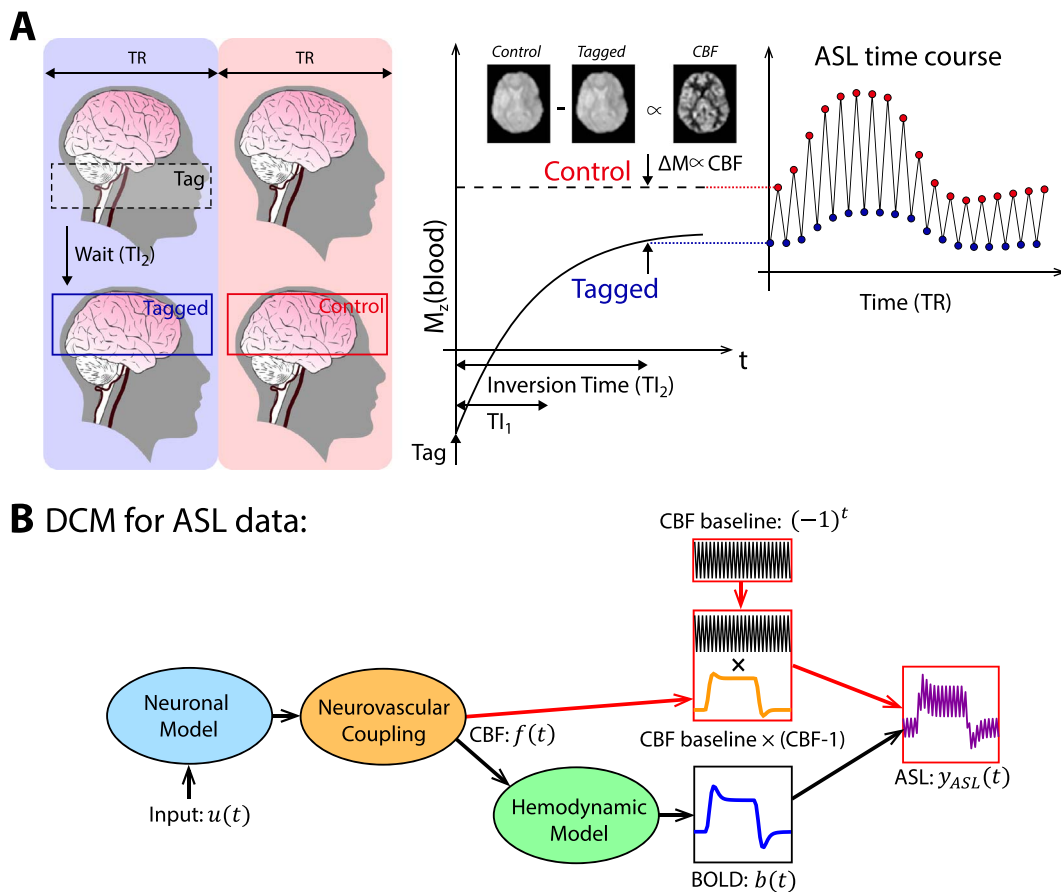
Fig. 2. (A) Illustration of the ASL data acquisition. The ASL pulse sequence involves labeling of the inflowing arterial blood proximal to the imaging slices by magnetic inversion (during inversion time, TI_1). Once the labeled blood, having its spins inverted, is delivered to the rest of the brain (after a certain inversion time, TI_2), it reduces the total signal magnitude in the subsequently acquired 'tagged' images. After collecting tagged images, the procedure is repeated without applying the magnetic inversion, and so called 'control' images are acquired while the inflowing blood is fully relaxed. Then dynamic alternation between acquiring tagged and control images gives the typical ASL measurement where the difference between control and tagged images is proportional to the local CBF and where the envelope represents the BOLD signal. (B) Schematic illustration of the ASL generative model for DCM that is common to all S-, 2S- and P-DCM. The output from NVC (i.e. CBF signal) and the BOLD signal are combined together with the CBF baseline to form the output ASL signal.

extracted from a sphere (radius 10 mm) centered at the peak T-value within each contrast image, and only voxels from grey matter (considering intersection of contrast images with the grey matter mask) were included. BOLD signals were derived from the ASL time-series using surround averaging (Mumford et al., 2006). Finally, the signal baselines of the BOLD time-series were identified from the initial and the last resting periods of each run and adjusted to zero[3].

Dynamic causal modeling

In this paper, we evaluate three DCM variants: standard, two-state and physiologically-informed DCM (S-, 2S- and P-DCM, respectively; please see Havlicek et al. (2015) and Supplementary material 1 for details). In the following, we also introduce DCM for ASL that allows one to perform model comparison for BOLD data alone or BOLD signal together with CBF. Hereafter, by stating "BOLD-data-alone", we refer to the analysis based only on the BOLD signal derived from ASL data. In contrast, by stating "ASL-data", we refer to the analysis performed directly on ASL data that includes both CBF and BOLD signal changes.

DCM of arterial spin labeling

ASL is an MRI approach that simultaneously measures CBF and BOLD signals (see Fig. 2A). Thus, ASL – in contrast to BOLD signal

alone – may provide additional information for studying neuronal dynamics and effective connectivity. We propose a full generative model of ASL data that extends the standard applications of DCMs for fMRI. In this model, we combine the GLM model of ASL signal described above (Hernandez-Garcia et al., 2010; Mumford et al., 2006; Woolrich et al., 2006), which has been shown to have fewer artifacts and increased sensitivity, compared to differencing and interpolation approaches, respectively, with physiological variables defined by hemodynamic models (Havlicek et al. 2015). The single-ROI output equation of the ASL-DCM is then given by:

$$y_{ASL}(t) = l_0 + l_1 \cdot (-1)^t + b(t) + l_2 \cdot (-1)^t \cdot (f(t) - 1) + \varepsilon(t). \quad (2)$$

where $y_{ASL}(t)$ is the ASL signal evaluated at time t. As in the ASL-GLM (see Eq. (1)), we model both MR and CBF signal baselines, whose effects are scaled by parameters l_0 and l_1, respectively. The CBF baseline has the same form as in the ASL-GLM. In contrast to ASL-GLM, the explanatory variable x_{BOLD} representing BOLD signal contribution to ASL signal is replaced by the output of the physiological BOLD signal model, $b(t)$ (see Figs. 1 and 2). Furthermore, the CBF contribution to the ASL signal is no longer approximated by x_{BOLD} but modeled directly using the output of the neurovascular coupling (NVC) in the physiological model (see Figs. 1 and 2); i.e., the blood flow state $(f(t)-1)$. Therefore, changes in the BOLD and CBF signals are caused by the changes in the same neuronal activity defined via input and connectivity parameters (see below). As in the ASL-GLM model, the CBF contribution, $(f(t)-1)$, is modulated by the CBF baseline due to the

---

[3] This is an important step if one wants to compare different DCMs, as these models are designed to model activity changes with respect to resting baseline.
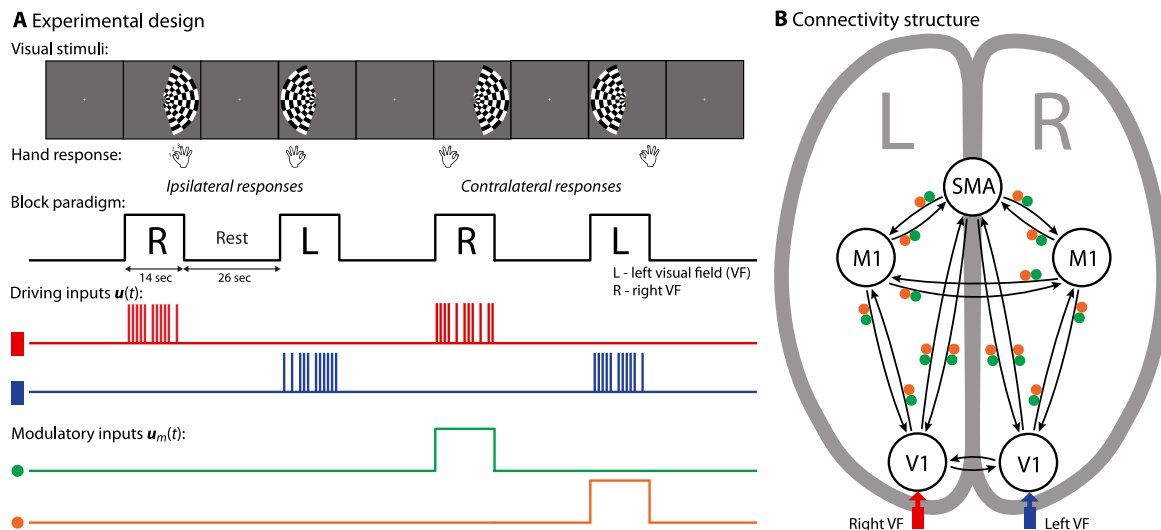
A Experimental design

Visual stimuli:

Hand response:

Ipsilateral responses   *Contralateral responses*

Block paradigm:

L - left visual field (VF)
R - right VF

Driving inputs $\boldsymbol{u}(t)$:

Modulatory inputs $\boldsymbol{u}_m(t)$:

B Connectivity structure

Right VF   Left VF

Fig. 3. Illustration of the experimental design of visuo-motor task (A) and connectivity architecture (B) assumed for the DCM model inversions. This illustrates the driving inputs entering the network of brain regions during left and right visual stimulation (red and blue colors) and modulatory inputs introducing changes to ipsilateral connectivity, while contralateral motor responses are enforced (green and orange colors).

alternating tag and control image acquisition in ASL. Since the contribution of CBF to the ASL signal varies as a function of the MR acquisition parameters, the CBF component is additionally scaled by the parameter l_2. Note that when l_1 and l_2 equal zero – that is no blood flow tagging and therefore no direct contribution of CBF to the measured signal – we obtain the standard BOLD model of DCM. In line with GLM (Friston et al., 1995), the error term $\varepsilon = \mathcal{N}(0, C_\varepsilon)$ models serially correlated noise by assuming an AR(1) plus white noise process encoded in the inverse covariance matrix $C_\varepsilon^{-1} = \sum \lambda_i Q_i$, where Q_i are known precision basis functions scaled by hyperparameters λ_i. An illustration of the ASL model for DCM is provided in Fig. 2B.

DCM analysis

We chose a visuo-motor experiment as an exemplary data-set to compare different DCM models and their physiological components. Note that the main aim of this paper is not to evaluate the best connectivity architecture for this task, but rather to show how different forms of neuronal and hemodynamic models impact connectivity estimates, under a plausible architecture. In other words, the experimental data serve to illustrate how different DCM variants account for neuronal and hemodynamic transients and how these variants influence connectivity estimates. Therefore, we selected a single connectivity architecture for all the DCMs that differ in their physiological mechanisms (see below). This connectivity structure was selected from several plausible candidates based on an initial BMS procedure; i.e., we selected the best architecture that explains the experimental data under all three DCMs (S-DCM, 2S-DCM and P-DCM). Further motivation for this architecture is provided in the Discussion.

Connectivity structure specification

A network of five brain regions – as illustrated in Fig. 3A – was used in our DCM analyses. For all DCMs, we used the bilinear form of the neuronal connectivity model[4]:

$$\frac{d\mathrm{x}_E(t)}{dt} = \left(\mathrm{A} + \sum\nolimits_{m=1}^{M} \mathrm{B}^{(m)} \cdot u_m(t) \right) \cdot \mathrm{x}_E(t) + \mathrm{C} \cdot \mathrm{u}(t). \qquad (3)$$

The network received driving inputs to the left or right V1, representing visual stimulation to the right or left visual fields, respectively (depicted in Fig. 3 with red and blue colors). The strengths of these inputs were encoded in the matrix C. Since we were only interested in evaluating differences in connectivity between ipsilateral and contralateral conditions (see Discussion), we associated the connectivity encoded in matrix A with the ipsilateral condition and modeled the effect of contralateral conditions using the B matrix. The regions were fully interconnected (depicted with black arrows) except for the two inter-hemispheric connections between right V1 and left M1 and between left V1 and right M1, which were omitted. To model changes in connectivity during contralateral conditions, we assume that all extrinsic connections in matrix A, except connections between left and right V1, could be modulated (depicted with green and orange dots). The implicit exclusion of modulatory effects between left and right V1 is based on prior BMS, where we compared models with and without these connections (see Discussion). Modulatory effects were encoded in the B matrix with two levels ($M = 2$): $\mathrm{B}^{(1)}$ for visual stimulation in the left visual field and $\mathrm{B}^{(2)}$ for visual stimulation in the right visual field. Therefore, the matrices B express the changes in connectivity due to switching motor output with respect to lateralized visual input. Modulation of extrinsic connections in the matrix A by the B matrices was controlled via modulatory inputs. These inputs were simple box-car functions that are ON during stimulation periods (see Fig. 3). This means that average connectivity during contralateral conditions is given by $\mathrm{A} + \sum_{m=1}^{2} \mathrm{B}^{(m)}$. In addition to the connectivity parameters, region-specific parameters of the hemodynamic models were optimized during the model inversion; please see Supplementary material 1.

Model inversion

All models (described in detail below) were inverted using Variational Laplace (VL), implemented for DCM in SPM12 (update R6470, (Friston et al., 2007)). In the VL approach, the moments (i.e. the parameter means and covariances) of the approximate posterior density $q(\theta) = \mathcal{N}(\eta, \mathrm{C})$ are iteratively updated to more closely approximate the true posterior distribution $p(\theta)$. This is achieved by maximizing a lower bound on the log model evidence:

---

[4] Note that Eq. (3) is displayed here in its general form, which lacks contribution of the inhibitory neuronal populations that are modeled in 2S-DCM and P-DCM. For a complete description of these models see Table S1.1 in the Supplementary Material 1.

$$\log p(y|m) = F(m) + KL(q(\theta)\|p(\theta|y,m)). \quad (4)$$

The model evidence, p(y|m), is the probability of obtaining the observed data, y, given the model, m, and is the cornerstone of Bayesian model selection (BMS). The first term, F(m), is the free energy (i.e. the lower bound) and the second term represents the Kullback-Leibler (KL) divergence between the approximate posterior density, q(θ), and the true posterior, p(θ|y, m). During the model inversion, maximizing F(m) implicitly minimizes the KL divergence, thus F(m) becomes an approximation to the model log-evidence.

Model inversions were performed individually for each subject and functional run, and separately for BOLD-data-alone and for ASL-data using the same prior distributions over model parameters (see Table S1.2). They all converged within 128 iterations. Note that while the modeled signal outputs for ASL data were represented by Eq. (2), the modeled BOLD signals for BOLD-data-alone were additionally convolved with a smoothing kernel [1 2 1]/4 in order to mimic the smoothing introduced by surround averaging (using the same kernel) to derive the BOLD signals from the ASL data (see also Supplementary material 1).

Analysis of the dependency of connectivity on model and data

To determine the dependency of connectivity strengths on the physiological assumptions of the three DCM models, we employed conditional parameter estimates (i.e. conditional means and (co) variances) to calculate group connectivity patterns provided by S-DCM, 2S-DCM and P-DCM. In particular, these were obtained using Bayesian model and parameter averaging (BMA and BPA) of extrinsic and intrinsic connectivity parameters, under FFX assumptions (Penny, 2012). Differences in averaged connectivity estimates were assessed between models for both ipsilateral and contralateral conditions.

To assess the similarity of the group connectivity estimates between BOLD and ASL-data for each DCM model, Pearson correlation coefficients were calculated between the average extrinsic connection strengths of BOLD-data-alone and ASL-data, respectively. Furthermore, to evaluate which data (BOLD-data-alone or ASL) provides more informed constraints on the underlying effective connectivity, we used the conditional posterior estimates of the three DCM models. Note that ASL-DCM cannot be directly compared with BOLD-DCM using BMS in terms of model log-evidence, because these two models are not fitted to the same data. However, posterior distributions of model parameters can be compared in terms of KL divergence between prior and posterior distributions. This KL divergence represents the part of model evidence that is directly related to model complexity (Penny, 2012). Hypothetically, one expects the prior and posterior distributions to diverge in a non-trivial fashion if there is sufficient information in the observed data to support the implicit increase in complexity. We restricted ourselves to prior and posterior distributions of extrinsic connectivity parameters – these are present in all DCMs for both BOLD-data-alone and ASL-data. Additionally, to address the same question from a different perspective, we used the KL divergence to calculate the number of effectively estimated parameters (NEP) (Penny, 2012) and to relate it to the actual number of free parameters (there are 44 parameters corresponding to the weights of extrinsic connections in each model).

Evaluating hemodynamic response fits

We calculated a subject-specific average BOLD response for each region and each condition in both measured and predicted BOLD time-courses. Further, using these averages, the percentage of explained response variance (PVE, also called coefficient of determination) for each brain region was determined. These PVE values were calculated at both the subject and group level. These constitute measures of accuracy that complement the KL complexity measures, described above.

For the full ASL-data, the average CBF and BOLD responses were calculated from a predicted ASL time-series by applying surround averaging and surround subtraction (Liu and Wong, 2005; Mumford et al., 2006) in order to mimic the same processing of measured ASL-data. For ASL, we also calculated PVE for both CBF and BOLD responses in each brain region.

Comparing model families

The above analysis focuses only on evaluating qualitative and quantitative differences between connectivity weights provided by the different models and their fits to the data. Here, we performed Bayesian model selection (BMS) (Penny et al., 2010) to compare S-, 2S- and P-DCM. In particular, we aimed to identify the relative importance of three new model components in P-DCM over their previous variants in S- and 2S-DCM (see Havlicek et al. (2015)). Therefore, three families within the space of model components were considered (see Table 1): the first family compared neuronal models, i.e. single-state vs. two-state vs. adaptive two-state neuronal model; the second family compared models of neurovascular coupling (NVC), i.e. feedback-based NVC vs. feedforward NVC; and the third family compared vascular mechanisms within hemodynamic models, i.e. coupled vs. uncoupled CBF-CBV relationship. This resulted in twelve different combinations of DCMs, where the Model 1 corresponds to S-DCM, Model 5 to 2S-DCM and Model 12 to P-DCM (see Table 1).

Based on the group log-evidence (i.e. log-evidence summed up over individual runs and subjects under fixed effects assumptions), the model with the lowest log-evidence was identified and then the relative log-evidences were determined among all twelve models listed in Table 1 (Penny et al., 2010). The model specific log-evidences were then used for family-wise BMS under fixed-effect (FFX) assumptions.

Table 1
Families of physiological model components.

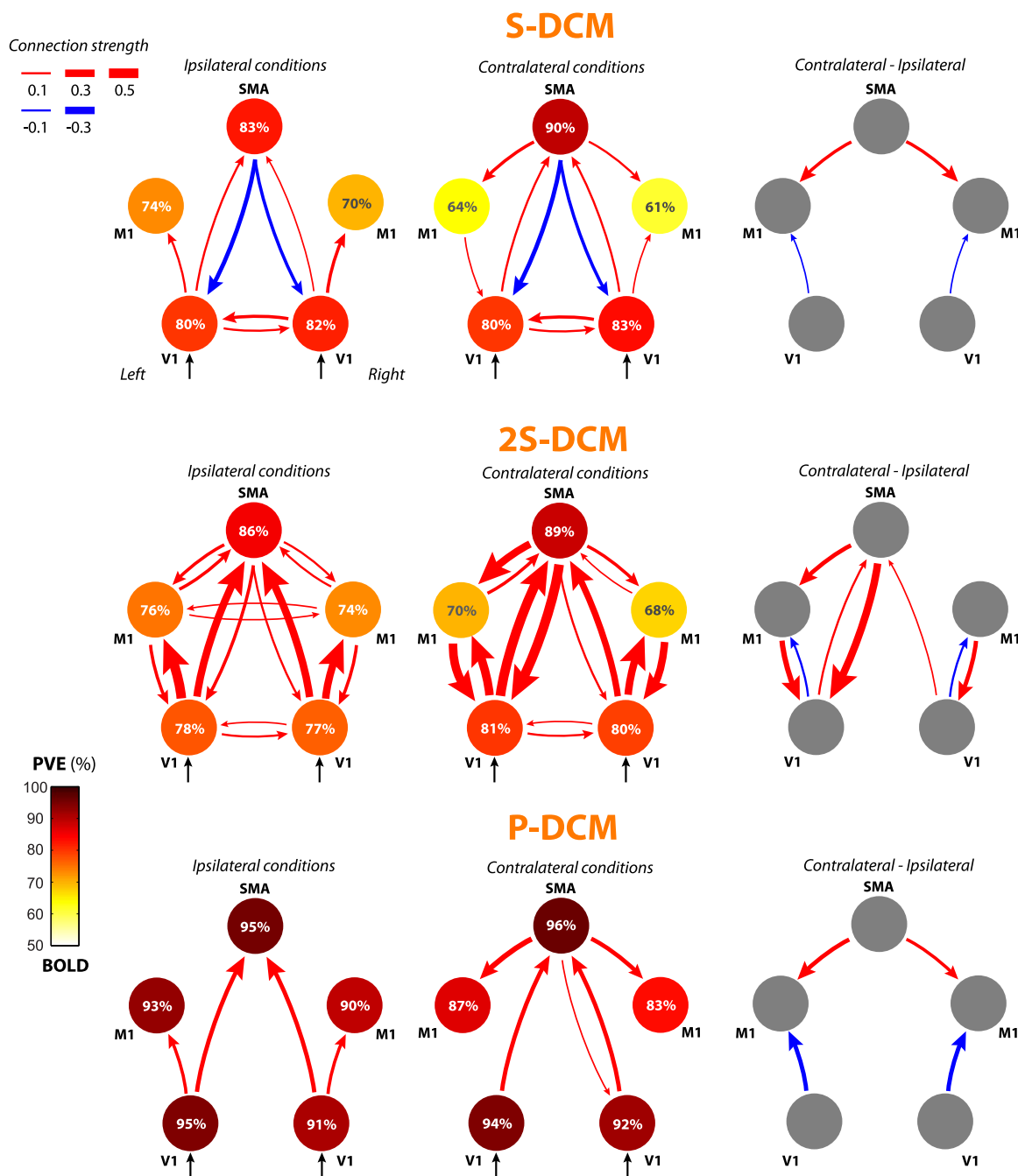| Model	Neuronal family			NVC family		Hemodynamic family	
	1-state	2-state	Adaptive 2-state	Feedback based NVC	Feedforward NVC	Coupled CBF-CBV	Uncoupled CBF-CBV
Model 1	•	–	–	•	–	•	–
Model 2	•	–	–	•	–	–	•
Model 3	•	–	–	–	•	•	–
Model 4	•	–	–	–	•	–	•
Model 5	–	•	–	•	–	•	–
Model 6	–	•	–	•	–	–	•
Model 7	–	•	–	–	•	•	–
Model 8	–	•	–	–	•	–	•
Model 9	–	–	•	•	–	•	–
Model 10	–	–	•	•	–	–	•
Model 11	–	–	•	–	•	•	–
Model 12	–	–	•	–	•	–	•

Fig. 4. Group connectivity results based on BOLD-data-alone estimated using S-DCM (top row), 2S-DCM (middle row) and P-DCM (bottom row). The left column depicts the endogenous connectivity during the ipsilateral conditions. The middle column shows modulation of the endogenous connectivity during the contralateral conditions. The right column displays the difference between ipsilateral and contralateral conditions; i.e. the effective change in connectivity due to the experimental manipulation. The causal direction and strength of the connection are depicted using an arrow and the line thickness, respectively. The positive connection weights between nodes are encoded with red color arrows and negative weights with blue color arrows (only absolute connection weights larger than 0.05 are shown). The region-specific PVE values are displayed within each node that is further color-coded based on the scale depicted in the color bar.

This provided posterior probabilities of specific model components within each model family; i.e., the likelihood that a certain model component is supported by the data. The relative model log-evidences and posterior probabilities were calculated for both BOLD-data-alone and ASL-data.

Results

How does the connectivity depend on the model and the data?

In the following, we describe group connectivity estimates (ob-

tained by BMA and BPA) using S-, 2S- and P-DCM, first for the BOLD-data-alone and later for the ASL-data. In Figs. 4 and 5 we show: (i) the average connectivity that is associated with signal changes observed during the ipsilateral conditions (i.e. connectivity matrix A, left column in Figs. 4 and 5); (ii) the average connectivity during contralateral conditions (i.e. connectivity matrix $A + \sum_{m=1}^{2} B^{(m)}$, middle column in Figs. 4 and 5); and (iii) the effective (condition-dependent) changes in connectivity due to experimental manipulation (i.e. the difference between ipsilateral and contralateral conditions, connectivity matrix $\sum_{m=1}^{2} B^{(m)}$, right column in Figs. 4 and 5). We encode positive connection weights between nodes with red color arrows and negative weights
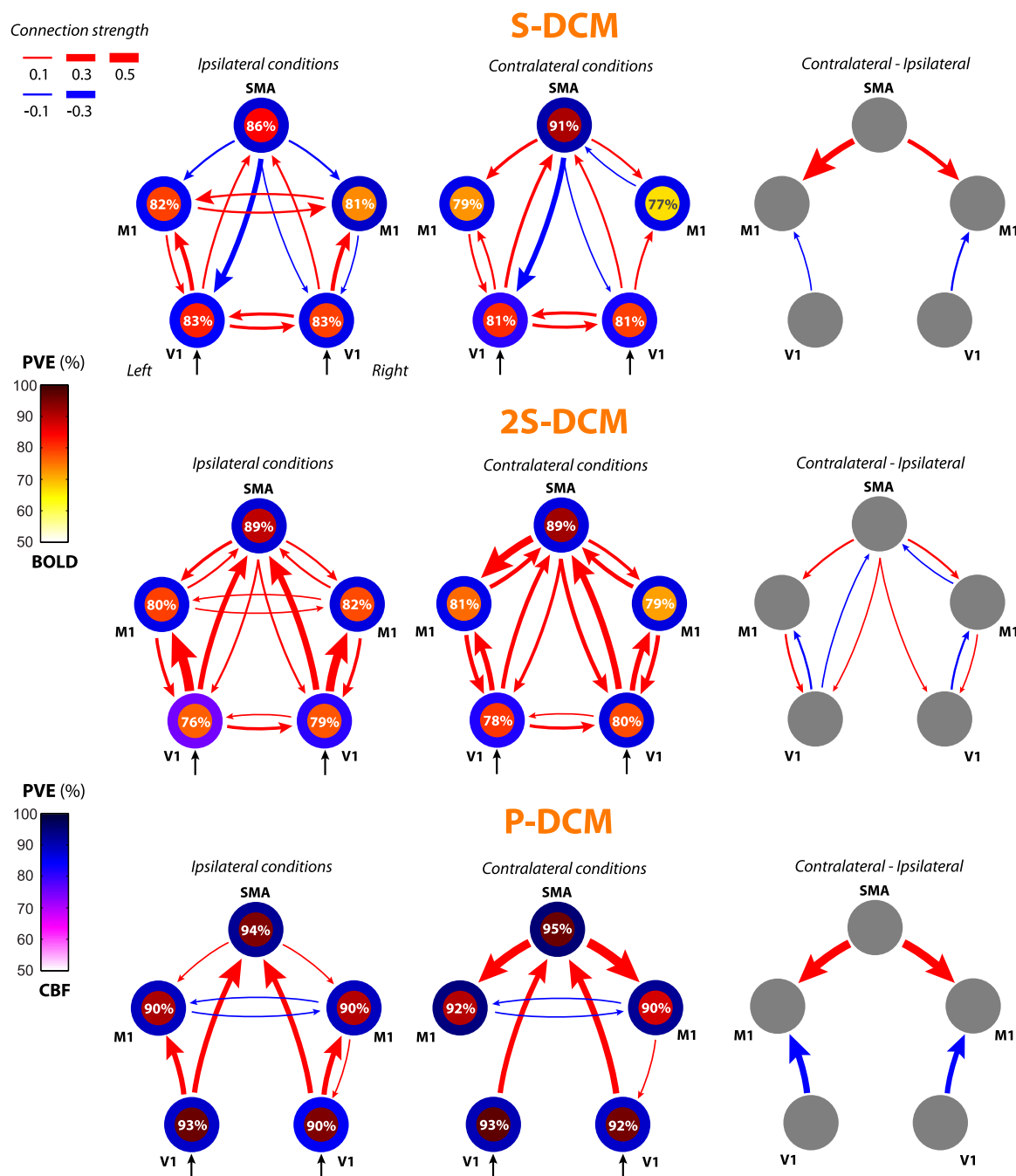
Fig. 5. Group connectivity results based on the ASL-data estimates. This figure adheres to the same description as Fig. 3 with the following exceptions: The PVE values are color-coded separately for CBF (purple-blue in the ring) and BOLD (yellow-red in the inner circle) responses in each of network node. The average PVE values of CBF and BOLD signal predictions are displayed within the nodes.

with blue color arrows (PVEs values color-code the central part of the nodes for the BOLD signal and outside ring for CBF, see details below). The direction and strength of the connection is depicted using an arrow and line thickness, respectively. We display only absolute connection weights larger than 0.05. For a complete set of connection weights see Table S1.3.

BOLD-data-alone

S-DCM connectivity results (see Fig. 4 top row) during the ipsilateral conditions show positive feedforward connections from left and right V1 to left and right M1, respectively, but also to SMA. In return, SMA influences both left and right V1 via strong negative feedback connections. Moreover, there are positive reciprocal connec-

tions between left and right V1. During contralateral conditions, the feedforward connections from left and right V1 to left and right M1, respectively, are mostly suppressed and additionally, stronger positive connections between SMA and left and right M1 emerged. The remaining connections are very similar to the ipsilateral conditions (see right column of Fig. 4).

In 2S-DCM connectivity results (see Fig. 4 middle row) during the ipsilateral conditions, we can see a fully connected network. As in S-DCM, the network is dominated by feedforward connections from left and right V1 to left and right M1, respectively, and to SMA. In contrast to S-DCM, all connections are positive and reciprocal. During contralateral conditions, feedforward connection strengths from left and right V1 to SMA are slightly increased and to left and right M1 are

decreased, but still strong. We can also notice a large increase in some of the feedback connections, such as from left and right M1 to left and right V1, respectively, and from SMA to left V1 and left M1.

P-DCM connectivity results represent a sparse network (see Fig. 4 bottom row). As in S-DCM, during ipsilateral conditions, we see positive feedforward connections from V1 to M1 and to SMA, but with stronger weights. In contrast to S-DCM, there are no negative feedback connections from SMA to left and right V1 and the reciprocal connections between left and right V1 are negligible. During contralateral conditions, the connections from V1s to M1s are completely suppressed and the activity propagates to contralateral M1s via connections from V1s to SMA and then via strongly enriched connections from SMA. Although the connectivity patterns seen with ipsilateral and contralateral conditions are different compared to S-DCM, the difference between these two conditions is similar to S-DCM (see right column of Fig. 4).

ASL-data (CBF & BOLD signal)

S-DCM results obtained from ASL-data (both ipsilateral and contralateral conditions) show similar connectivity patterns as obtained from BOLD-data-alone (see Figs. 5 and 4, top row), albeit with some qualitative and quantitative differences. The Pearson correlation coefficient between connectivity patterns estimated using BOLD-data-alone and ASL-data (only extrinsic connections included) is 0.8967 (see Table 2). The main differences are in the strength of significant connections. Some connections exhibit much higher strengths in the case of ASL data. For example, using ASL-data, positive connections between left, right V1 and left, right M1 are ~1.6 times stronger during ipsilateral conditions and ~2.7 times stronger during contralateral conditions as compared to BOLD-data-alone. Additionally, negative connections from SMA to left and right M1 during ipsilateral conditions, which are negligible in BOLD-data-alone, are ~4.3 times stronger if ASL-data are used. It is worth noting that many subthreshold connections (not displayed in Figs. 4 and 5) have weights closer to zero (see Table S1.3). The difference between conditions is generally comparable to BOLD-data-alone (see right column of Fig. 5).

2S-DCM connectivity results based on ASL-data are again not too different from those based on BOLD-data-alone (Figs. 5 and 4, middle row). The Pearson correlation coefficient between connectivity patterns based on BOLD-data-alone and ASL-data is 0.8532, which is slightly lower than for S-DCM. In general, most connection strengths estimated from ASL-data are slightly weaker compared to estimates based on BOLD-data-alone. This is an opposite effect compared to the results based on S-DCM. The largest discrepancy between estimated connectivity by BOLD-data-alone and ASL-data can be seen in between condition differences. There is slightly more similarity to S-DCM results in the condition differences provided by ASL-data than when BOLD-data-alone is used (see Figs. 4 and 5).

P-DCM results obtained from ASL-data (both ipsilateral and contralateral conditions) strongly resemble the sparse connectivity patterns as obtained from the BOLD-data-alone (Figs. 5 and 4, bottom row). The Pearson correlation coefficient between connectivity patterns based on BOLD-data-alone and ASL-data is 0.9576; i.e. higher than both S-DCM and 2S-DCM. The main noticeable difference to BOLD-data-alone results is in the overall higher strength of significant connections for ASL-data. For example, connections from V1s to M1s are ~1.7 times stronger; connections from V1s to SMA are ~1.2 times

stronger; and connections from SMA to M1s are ~1.9 times stronger.

How does the model explain hemodynamic responses in multiple areas?

PVE values are encoded in the color of network nodes for the BOLD signal and outer rings for CBF (Figs. 4 and 5). Individual subjects and group average PVE values for both BOLD-data-alone and ASL-data can be found in Table 3. Average responses of the observed data and fitted responses (from a single subject) are displayed in Figs. 6 and 7.

BOLD-data-alone

For S-DCM, the region-specific PVE values range between 61% and 90%. This wide range of PVE values can be explained by the predicted single-subject BOLD responses (red lines in Fig. 6). The positive peaks of hemodynamic responses, including their delays, are well explained during ipsilateral conditions. However, during contralateral conditions, the positive response in left M1 is significantly delayed with respect to the measured BOLD data. Furthermore, S-DCM was mostly able to explain negative responses in M1 regions during both ipsilateral and contralateral conditions. Although S-DCM fits the post-stimulus undershoot in left M1 during ipsilateral conditions, it only provides a partial explanation of the undershoot in left and right V1s and right M1 areas during contralateral conditions (see Fig. 6); i.e. explained variance reduces during the contralateral conditions. We note that when S-DCM fits the post-stimulus BOLD undershoot well in a certain brain area (e.g. left M1 during ipsilateral condition), then there are stronger negative feedback connections targeting the area in question (see Supplementary material 2).

PVE range for 2S-DCM is between 68% and 89%. 2S-DCM fits the positive peaks of hemodynamic responses with similar accuracy as S-DCM (cyan lines in Fig. 6). In contrast to S-DCM, the two-state neuronal model cannot explain contralateral negative responses in M1 areas. Furthermore, the majority of post-stimulus BOLD undershoots are under-fitted, resulting in lower PVE values than S-DCM (see Table 3).

P-DCM generally scores higher PVE values in all regions, ranging between 83% and 96%, but the majority is above 90%. P-DCM was able to fit the positive peak of BOLD responses more accurately than S-DCM and 2S-DCM, especially during rising and falling phases of the hemodynamic response. As with S-DCM, P-DCM explains negative

Table 3.
Average PVE values for individual subjects and entire group.

	S-DCM	2S-DCM	P-DCM
BOLD (alone):			
Subject 1	80.27 ± 4.12	81.14 ± 3.47	92.55 ± 2.16
Subject 2	78.34 ± 3.83	74.98 ± 3.64	92.14 ± 2.36
Subject 3	77.14 ± 4.66	78.22 ± 2.51	94.85 ± 1.49
Subject 4	72.43 ± 3.66	73.70 ± 4.84	88.03 ± 2.66
Subject 5	76.23 ± 4.42	77.67 ± 3.71	90.35 ± 2.30
Group average	**76.89 ± 4.20**	**77.13 ± 3.75**	**91.58 ± 2.28**
BOLD (ASL):			
Subject 1	75.50 ± 4.55	75.94 ± 4.39	93.72 ± 1.93
Subject 2	80.91 ± 2.59	80.84 ± 3.04	95.19 ± 0.97
Subject 3	82.80 ± 2.08	87.07 ± 1.85	95.22 ± 1.49
Subject 4	73.36 ± 3.48	76.63 ± 3.45	90.80 ± 2.21
Subject 5	78.07 ± 3.79	77.86 ± 4.36	91.48 ± 2.11
Group average	**78.89 ± 3.50**	**79.69 ± 3.66**	**93.27 ± 1.85**
CBF (ASL):			
Subject 1	85.02 ± 3.36	82.65 ± 2.28	88.65 ± 3.44
Subject 2	90.22 ± 2.43	86.48 ± 3.88	92.53 ± 2.45
Subject 3	91.43 ± 1.29	90.75 ± 1.73	94.54 ± 1.29
Subject 4	82.79 ± 3.66	81.10 ± 3.54	90.36 ± 2.51
Subject 5	80.05 ± 4.83	73.11 ± 5.18	86.36 ± 3.54
Group average	**85.92 ± 3.47**	**82.81 ± 3.78**	**90.49 ± 2.84**

Table 2
Correlation between connectivity weights of BOLD-data-alone and ASL-data.

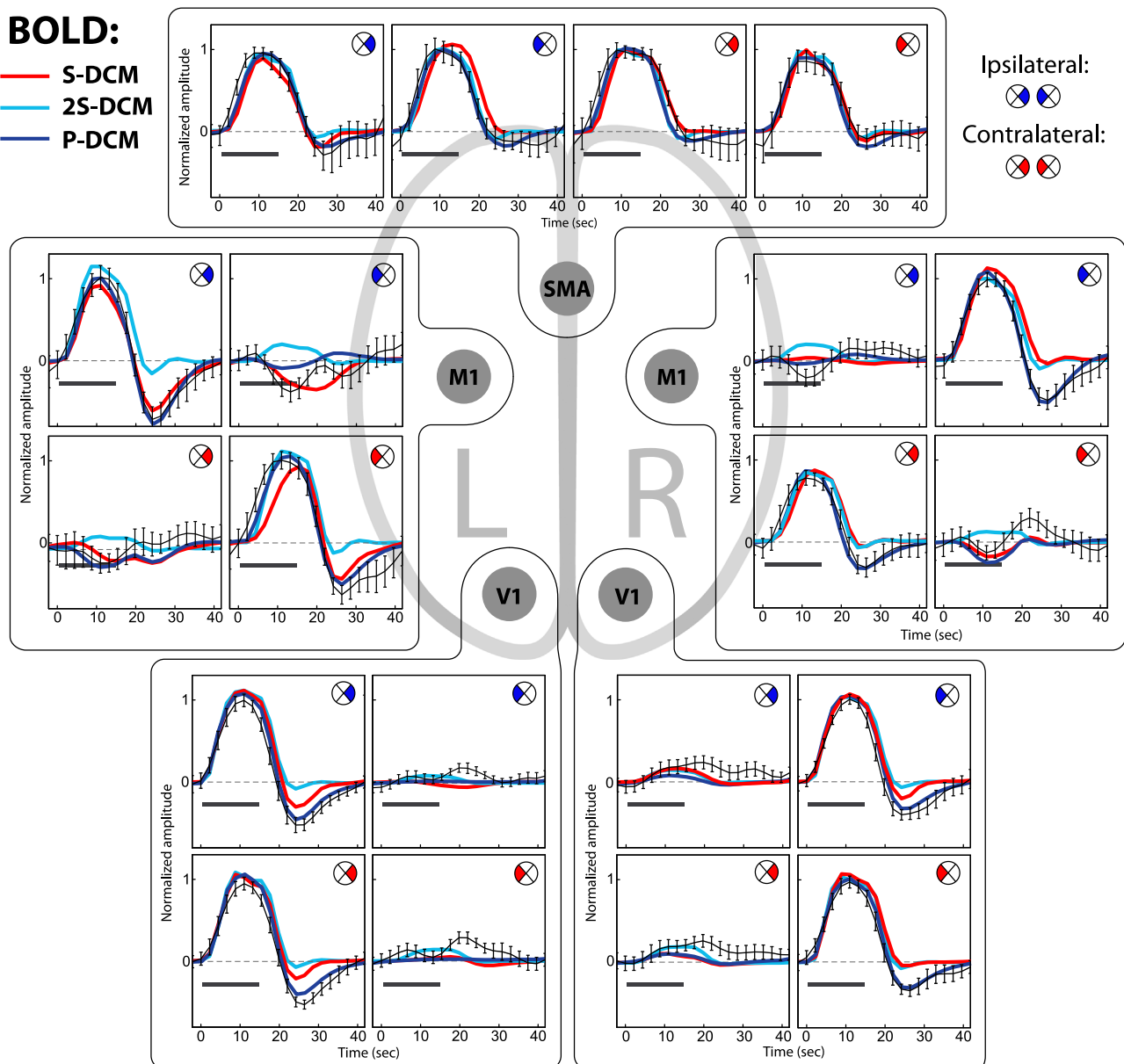|	S-DCM	2S-DCM	P-DCM
	BOLD vs. ASL	**BOLD vs. ASL**	**BOLD vs. ASL**
Correlation	0.8967	0.8532	0.9576

Fig. 6. Single-subject average region-specific hemodynamic responses fitted by S-DCM, 2S-DCM and P-DCM to BOLD-data-alone. The observed BOLD responses for both ipsilateral and contralateral conditions are displayed with solid black lines, including error bars that represent the 95% confidence interval. The laterality of the visual stimulation is marked in the upper right corner of each plot with a colored wedge (blue color represents ipsilateral hand response and red color contralateral hand response). The BOLD responses fitted by S-DCM, 2S-DCM and P-DCM are displayed using solid red, cyan and blue lines, respectively. Region-specific responses are normalized with respect to the maximum amplitude of the observed responses across all conditions, i.e. the proportional differences in amplitudes between conditions are preserved.

responses in contralateral M1 areas (blue lines in Fig. 6). Finally, P-DCM explains post-stimulus BOLD undershoot with high accuracy in all five brain regions during both ipsilateral and contralateral conditions. Importantly, compared to S-DCM, P-DCM fits post-stimulus BOLD undershoots without relying on extrinsic negative feedback connections (see Fig. 4 and Supplementary material 2); i.e., using local neuronal and hemodynamic mechanisms.

ASL-data (CBF & BOLD)

In Fig. 5, the PVE values are color-coded separately for CBF (purple-blue in the outer ring) and the BOLD signal (yellow-red in the inner circle) responses in each of network node. The average PVE values of CBF and BOLD signal predictions are displayed within the nodes.

For S-DCM, PVE values for the BOLD responses are between 65% and 89%, which is slightly higher than in the case of BOLD-data-alone.

However, the majority of post-stimulus undershoots in BOLD responses are not well explained. On the other hand, PVE values for the CBF responses are between 81% and 91%. Thus, in majority of cases, CBF responses have surprisingly higher PVE values than BOLD predictions in ASL data given that CBF data typically are noisier than BOLD signals. In terms of single-subject predictions of CBF responses (orange lines in Fig. 7), the post-stimulus deactivations are fitted with high accuracy.

In 2S-DCM results, the PVE values for BOLD predictions are between 72% and 92%. BOLD response predictions are comparable to predictions based on BOLD-data-alone – here 2S-DCM does not explain post-stimulus undershoots (see Figs. 6 and 7). For CBF predictions, PVE values are between 73% and 89%. CBF predictions provide moderately accurate fits to the measured CBF responses, including post-stimulus deactivations; with lower PVE values compared to S-DCM (see Figs. 4 and 5). It can be seen that the CBF
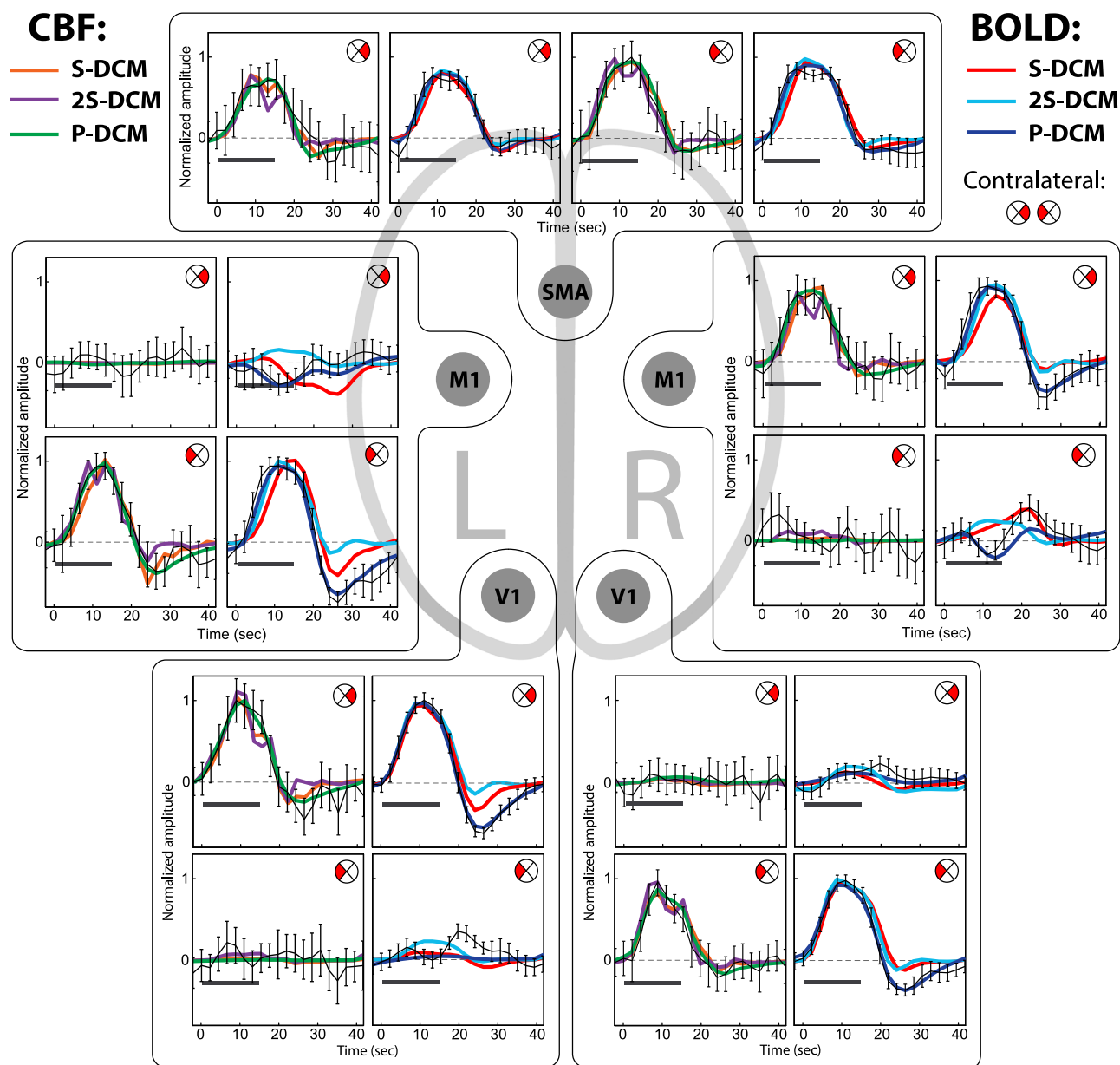
Fig. 7. Single-subject average region-specific hemodynamic responses fitted by S-DCM, 2S-DCM and P-DCM to ASL-data. Organization of this figure is the same as in Fig. 6 except that only responses to contralateral conditions are displayed. Observed CBF responses are displayed on the left of the BOLD responses. These are overlaid with the CBF response predicted by S-DCM, 2S-DCM and P-DCM, depicted with solid orange, purple and green colors, respectively.

predictions of 2S-DCM are more 'wrinkled' compared to S-DCM (purple lines in Fig. 7). Negative contralateral responses in M1 are not explained at the CBF or BOLD signal level.

In P-DCM results, the PVE values for BOLD predictions range between 88% and 97%, which is somewhat higher than PVE values scored with BOLD-data-alone (see Table 3). More accurate fits of BOLD responses using ASL-data compared to BOLD-data-alone reflect even more precise fitting of the post-stimulus BOLD undershoots. CBF predictions have also higher PVE values compared to S-DCM and 2S-DCM, ranging between 85% and 95%. In contrast to S-DCM and 2S-DCM, these are – in the majority of cases – slightly lower than for BOLD predictions. In short, P-DCM provides the most accurate fits of CBF and BOLD responses compared to 2S-DCM and 2S-DCM (green lines in Fig. 7).

Does model inversion benefit from ASL-data?

From the model inversion perspective, all three models (S-, 2S- and

Table 4
KL divergence and number of effectively estimated connectivity parameters (NEP).

	S-DCM		2S-DCM		P-DCM	
	BOLD	**ASL**	**BOLD**	**ASL**	**BOLD**	**ASL**
KL divergence	250.69	258.89	163.77	171.27	248.76	253.38
NEP (N=44)	84.74	86.94	55.00	57.51	84.20	85.29

P-DCM) benefit from additional information in ASL-data, as the KL divergence between prior and posterior distributions of extrinsic connections is always larger for ASL-data (see Table 4). This means that the posterior distribution departs more significantly from the prior distribution using ASL-data than using BOLD-data-alone. NEP and KL divergence scored by P-DCM is very close to S-DCM, which has the highest NEP and KL divergence scores. The same information gain is reflected in the number of effectively estimated parameters, which is always higher for ASL-data and generally higher than the actual

number of free parameters. Note that the ASL generative model has in general two additional free parameters in the output signal model (plus one more in the feedforward NVC) per ROI compared to the DCM for BOLD signals. Moreover, the adaptive neuronal model embedded in P-DCM has one more free parameter compared to S-DCM and 2S-DCM per ROI. The higher number of free parameters in the model can, in principle, result in the lower confidence about the estimates of connectivity weights, hence in a smaller departure from the prior distributions. This suggests that observed increase in KL divergence (by ~7) or in NEP (by ~2) in the case of ASL-data (i.e. higher confidence about the estimates) represents a significant improvement.

Which is the best model and how does it depend on the data?

Fixed effect Bayesian model selection performed on posterior parameter estimates, obtained by fitting models to BOLD-data-alone, over all individuals revealed that P-DCM (Model 12) had the highest relative log-evidence, outperforming the S-DCM (Model 1) and 2S-DCM (Model 5) by very strong[5] log-evidence differences $\Delta F = 1705$ and $\Delta F = 1411$, respectively (see Fig. 8A). Log-evidence differences are consistently very large also at the level of individual subjects (see Table 5). Overall, this results in posterior probability > 99% for BOLD-data-alone being compatible more with data predicted by P-DCM rather than by S- or 2S-DCM. Furthermore, comparing S-DCM and 2S-DCM using BOLD-data-alone showed strong log-evidence difference ($\Delta F = 294$) in favor of 2S-DCM, which confirms previous results (Marreiros et al., 2008).

Results obtained by comparing the same models using ASL-data revealed even more striking differences (see Fig. 8B). Here, the differences in log-evidence are more than 1.5 times larger than in the case of BOLD-data-alone. In particular, P-DCM is chosen over S-DCM and 2S-DCM with very strong log-evidence differences $\Delta F = 2855$ and $\Delta F = 3243$, respectively. In contrast to BMS results obtained using BOLD-data-alone, ASL-data favors S-DCM over 2S-DCM ($\Delta F = 388$).

At the level of model families, all three new model components of P-DCM; i.e., the adaptive two-state neuronal model, the feedforward NVC, and the CBF-CBV uncoupling, are very strongly supported by the family comparison with posterior probability > 99%. This was the case for both BOLD-data-alone and ASL-data (see Fig. 8A and B, bottom panels). In general, models that include the adaptive two-state neuronal model brought the largest model improvement (Models 9-12), scoring a larger log-evidence than models without this component (Models 1-8). Models that include CBF-CBV uncoupling (Models 2, 4, 6, 8, 10, 12) were also always supported over competing models where CBF-CBV is coupled (Models 1, 3, 5, 7, 9, 11). Considering the feedforward NVC instead of the feedback based NVC results in moderate differences in log-evidence. Note that not all models benefit from modeling this physiological mechanism. While for P-DCM the feedforward NVC increases log-evidence for both coupled and un-coupled CBF-CBV scenarios (see Models 11-12 vs. Models 9-10 for both BOLD-data-alone and ASL-data), removing feedback in S-DCM and 2S-DCM can result in decrease of log-evidence (see Models 3 vs. Models 1 and Models 7-8 vs. Model 5-6, respectively, for BOLD-data-alone). However, in the case of ASL-data, S- and 2S-DCM both benefit from the feedforward NVC if used together with the CBF-CBV uncoupling.

Discussion

In this paper, we compared the recently described P-DCM (Havlicek et al., 2015) with S-DCM and 2S-DCM to model effective connectivity in a network of brain regions. We demonstrated that

---

[5] Usually, a difference in log-evidence above three is considered as strong evidence (Kass and Raftery, 1995).
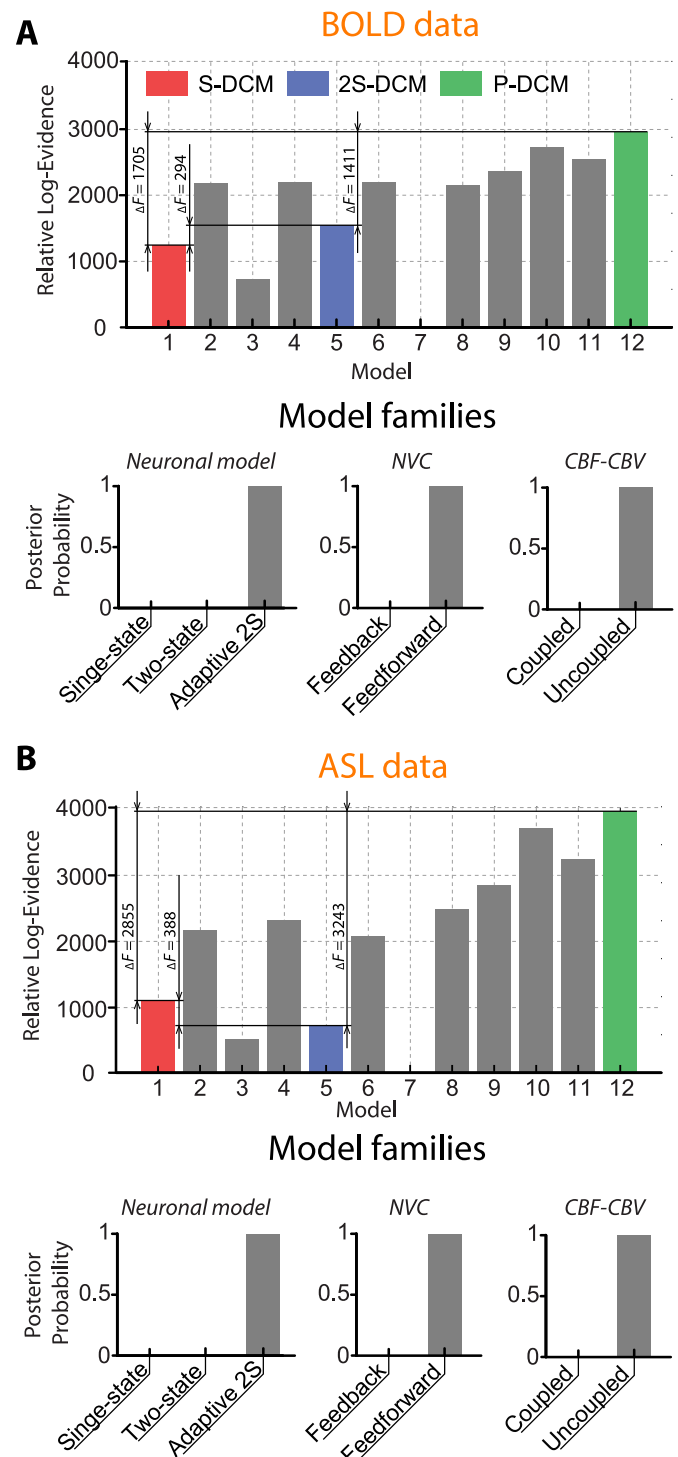

Fig. 8. Summary of the Bayesian model comparison results for BOLD-data-alone (A) and ASL-data (B). The figure compares twelve DCMs resulting from the factorial structure of family-wise comparison between the generative model components (i.e. single-state vs. two-state vs. adaptive two-state neuronal model, feedback vs. feedforward NVC, coupled vs. uncoupled CBF-CBV relationship) as described in Table 1. The first row shows the relative model log-evidence summed across all subjects (i.e. the model log-evidence minus the log-evidence of the reference model). The second row displays posterior probability of each model component within a specific model family (i.e. neuronal model, NVC, CBF-CBV relationship). The same description applies to the results from the ASL-data.

accurately modeling the response transients – using different physiological mechanisms – significantly affects effective connectivity estimates between functionally activated brain areas. The extension of

Table 5
Log-evidence difference between competing models.

	P-DCM vs. S-DCM		P-DCM vs. 2S-DCM		S-DCM vs. 2S-DCM	
	BOLD	**ASL**	**BOLD**	**ASL**	**BOLD**	**ASL**
Subject 1	408	795	333	754	-75	-41
Subject 2	220	568	342	792	122	224
Subject 3	594	719	297	649	-297	-70
Subject 4	49	324	31	427	-18	103
Subject 5	434	449	408	621	-26	172
Total	**1705**	**2855**	**1411**	**3243**	**-294**	**388**

DCM for the ASL MRI sequences – measuring both CBF and BOLD signals – allowed model comparisons using both BOLD-data-alone, as is typically used in DCM studies, and ASL-data. This (together with Bayesian model selection) furnished further evidence for the ability of P-DCM to disentangle neuronal and vascular parameters, which speaks to the contribution of the physiological mechanisms implemented in the respective generative models.

P-DCM differs from S-DCM and 2S-DCM in the following physiological model features: adaptation of the neuronal response by local inhibitory population; feedforward NVC; and possibility of CBF-CBV uncoupling (see Fig. 1). In a previous paper (Havlicek et al., 2015), we have evaluated the impact of these mechanisms on fitting single ROI time-courses and established their physiological relevance. However, all these features may also influence connectivity estimates when they are applied jointly with the bi-linear DCM neuronal connectivity model. This is because, in model inversion, any model component lying between the neuronal level and the output fMRI signal (i.e. the biophysical model) can have an effect on estimated neuronal signals (Roebroeck et al., 2011; Valdes-Sosa et al., 2011).

BOLD-data-alone

DCM is most often applied to BOLD fMRI data using S-DCM (Friston et al., 2003; Seghier, 2010). Based on a standard FFX Bayesian procedure for model selection (Penny et al., 2010), our results provided clear evidence that for the given BOLD data, P-DCM is statistically by far the superior model in comparison to S-DCM and 2S-DCM; not only for single regions, as shown in the previous paper (Havlicek et al., 2015)), but also for estimating connectivity in a network. This was demonstrated through very large log-evidence differences between P-DCM and the other two models ($\Delta F = 1705$ and $\Delta F = 1411$ with respect to S-DCM and 2S-DCM, respectively). These results also showed that for BOLD-data-alone, 2S-DCM is a better model than S-DCM, confirming previous BMS results (Marreiros et al., 2008). Note that, in general, difference in log-evidence $\Delta F > 3$ is considered as strong evidence (Kass and Raftery, 1995).

These large differences in log-evidence are mainly due to substantial fitting errors with S-DCM and 2S-DCM, which are unable to accurately explain the form of hemodynamic responses (see below). As we have shown previously (Havlicek et al., 2015), P-DCM includes basic physiological mechanisms that are necessary to account for the repertoire of measured BOLD responses, that are insufficiently modeled by S-DCM and 2S-DCM. This is further supported by the fact that the log-evidence is accumulated (summed up) over five subjects (each with 4 runs and 382 data points per run), thus allowing for very powerful inference. The log-evidence differences for a single functional run ranged from 30 to 120. Differences of this magnitude between log-model evidences have been reported before (Marreiros et al., 2008; Rosa et al., 2011; Stephan et al., 2007), even in cases where the compared models had rather subtle differences in physiological mechanisms (or their impact on the shape of hemodynamic response function was small).

Next, by performing model comparison at the level of model families (Penny et al., 2010), we were able to show that all three new components of the generative model as implemented in P-DCM (i.e. adaptive two-state neuronal model; feedforward NVC; and CBF-CBV uncoupling) are statistically superior to their previous counterparts (see Fig. 8 for family comparison of posterior probabilities). This means that all the physiological mechanisms as proposed in (Havlicek et al., 2015) are well supported by the experimental BOLD data and they are suitable for modeling both single and multiple ROI fMRI data.

Examining the connectivity pattern obtained by the different DCMs, the endogenous connectivity estimates (see ipsilateral conditions in Fig. 4) were different for all three models applied to the same data. While 2S-DCM yielded a fully connected network, connectivity estimated by P-DCM is sparse, including only positive connections. S-DCM provided a less sparse network with additional negative feedback connections. Nevertheless, the actual changes in connectivity weights due to experimental manipulation (i.e. difference between ipsilateral and contralateral conditions) are similar between S-DCM and P-DCM, yet differ remarkably from 2S-DCM. Note that a larger agreement between S-DCM and P-DCM in connectivity modulation is well expected, because they share the same neuronal model for long-range connections. On the other hand, larger differences in endogenous connectivity are related to different physiological mechanisms embedded in S-DCM and P-DCM, because this connectivity generates neuronal responses also outside stimulation periods (Friston et al., 2003; Stephan et al., 2008). Therefore, it can reflect local temporal variation often seen in both neuronal and hemodynamic responses, such as post-stimulus deactivation and undershoot (Gonzalez-Castillo et al., 2012; Hoge et al., 1999). The reason why connectivity estimates provided by 2S-DCM differ dramatically from S-DCM and P-DCM is due to different assumptions about extrinsic connections, which are forced to be positive (excitatory) by log-normal transformation[6] (Marreiros et al., 2008; Stephan et al., 2008). In contrast to our results, Stephan et al. (2007) showed that the neuronal connectivity parameters are fairly robust to changes in the output form of BOLD signal equation. Mechanisms compared in our paper (i.e. neuronal models, NVCs, CBF-CBV couplings) have a much greater impact on the shape of BOLD response function and thus can result in larger differences.

To further examine the observed differences in connectivity estimates provided by different models, we have carefully evaluated how well each model fits region-specific BOLD responses (see Fig. 6). Although comparing the accuracies of model fit is not a sufficient measure to determine which model is better or more useful (Friston et al., 2013), examining the accuracy (that is part of the log-evidence) next to the BMS can help us draw a more detailed (quantitative) picture about the model performance and its physiological relevance. The majority of BOLD responses associated with the five nodes of the network exhibit strong hemodynamic transients in the form of post-stimulus undershoot (see Fig. 6). These transients in observed hemodynamic responses – possibly caused by neuronal and/or vascular physiological mechanisms – are repeatedly reported (e.g. see (Chen and Pike, 2009; Hoge et al., 1999; Logothetis and Wandell, 2004; Mandeville et al., 1999; Sadaghiani et al., 2009; Shmuel et al., 2002)). Our results showed that P-DCM explains a larger variance of the hemodynamic response in all regions, compared to the other models, with average PVE values of ~91% (see Table 3). Both S-DCM and 2S-DCM achieved considerably lower PVE values (~77%), resulting mostly from under-fitted post-stimulus BOLD undershoots. Note that the post-stimulus undershoot can be in some extreme cases almost as large as the main positive BOLD response (see Fig. 6). S-DCM was able

---

[6] Note that while S-DCM and P-DCM have the prior means on connections equal zero, 2S-DCM due to the log-transform has the prior mean equal to 1/8. In general, this can result in more non-zero connections if the evidence from the data does not give enough support that these connections should be actually zeros (i.e. scaling parameters involved in log-transforms have to be strongly negative).

to explain post-stimulus undershoot in some regions, but 2S-DCM was more accurate in fitting the rising phase of the positive BOLD response.

In P-DCM, the presence of post-stimulus undershoot may be explained by a local adaptation mechanism in inhibitory populations (i.e. conceptually in line with e.g. (Mullinger et al., 2013; Sadaghiani et al., 2009)) and by uncoupling between CBF and CBV (i.e. in accordance with e.g. (Buxton et al., 1998; Chen and Pike, 2009; Havlicek et al., 2017; Mandeville et al., 1999)), resulting in sparser endogenous connectivity. Since S-DCM does not include these local physiological mechanisms, it naturally attempts to model the variation in neuronal/hemodynamic response, not explainable by local physiological processes, by long-range excitatory connections. Therefore, we see stronger negative feedback connections that cause more pronounced post-stimulus response deactivation (at the neuronal level) and undershoot (at the BOLD signal level). Note that the general mechanism of negative feedback-based NVC used by both S-DCM and 2S-DCM may in principle modulate post-stimulus BOLD signal timecourse as well. However, as we have shown earlier (Havlicek et al., 2015), for longer stimulus durations (as in our paradigm), this modulation is minimal – even with large variation of the decay parameter κ controlling the flow inducing signal. Furthermore, even though 2S-DCM possesses a mechanism to locally control excitatory activity by the inhibitory population within the two-state model, its parameterization is ineffective in explaining a wide range of neuronal/hemodynamic response transients (see Fig. 6, and see also Havlicek et al. (2015)). Put simply, fitting errors due to physiologically less plausible mechanisms implemented in S-DCM and 2S-DCM can be partially compensated by endogenous connectivity estimates. Moreover, it is important to remember that the log-evidence accounts for both model fit accuracy and model complexity (Penny, 2012). That is, a good model has to be accurate and still reasonably simple (in terms of the number of free parameters) in order to win the Bayesian model comparison. In this respect, P-DCM can accurately fit the entire shape of hemodynamic response with only a low or negligible increase in complexity (measured with KL divergence and NEP, see Table 4) compared to S-DCM.

The finding that the endogenous connectivity in S- and 2S-DCM is possibly more susceptible to hemodynamic variations, while the additive (or multiplicative (Stephan et al., 2008)) changes in connectivity due to experimental manipulation are not, agrees with the original characterization of connectivity S-DCM (Friston et al., 2003). Indeed, one of the main recommendations for DCM analysis is to design experimental modulations of endogenous connectivity couplings (Roebroeck et al., 2011; Stephan et al., 2010). However, there are situations, especially in clinical studies, which call for comparing endogenous connectivity between two different groups (e.g. controls vs. patients) (Agosta et al., 2010; Crossley et al., 2009; Miyake et al., 2010; Rocca et al., 2007). In addition, DCM analysis has been recently developed for resting-state data (Friston et al., 2014), which inherently assumes only endogenous connectivity. Therefore, in these cases, connectivity estimates provided by S-DCM and 2S-DCM may be more susceptible to variations of vascular (in addition to neuronal) signals than P-DCM.

In summary, results based on BOLD-data-alone suggest that models in S-DCM and 2S-DCM may be too restrictive for certain hemodynamic changes (e.g. adaptation and post-stimulus undershoot) observed in many fMRI experiments. P-DCM, in comparison, provides a more sparse connectivity accompanied with a locally-rich repertoire of neuronal and hemodynamic processes, which is statistically supported by the experimental data used in this study. Additionally, compared to S-DCM, P-DCM provides significantly more stable connectivity estimate across subjects and functional runs (see Supplementary material 2 for more details).

ASL-data

The DCM framework is not limited to BOLD-data-alone but can also be extended to ASL fMRI data (and other hemodynamic measures,

such as CBV), which simultaneously measures CBF and BOLD signal. In this study, we have developed such an extension, which enabled us to estimate effective connectivity and perform model comparisons also with ASL data.

BMS on ASL-data revealed even stronger log-evidence differences in favor of P-DCM. In contrast to BMS results obtained using BOLD-data-alone, ASL-data favors S-DCM over 2S-DCM. Therefore, one can speculate that 2S-DCM might be a better model for BOLD data than S-DCM from a statistical point of view (as summarized by BMS) but not from physiological point of view, when constrained with CBF. The model comparison at the family level confirmed the results from BOLD-data-alone, but ASL-data further showed that both S- and 2S-DCM can benefit from the feedforward NVC and the CBF-CBV uncoupling, if used together. The KL divergence between prior and posterior distributions of extrinsic connections (and NEP) showed that parameter estimation in all models benefit from ASL data (i.e. from additional CBF component) compared to BOLD-data-alone, even though the generative model for ASL-DCM has higher number of free parameters (see Method section and Table 4).

We have shown that the connectivity estimates for DCM variants using ASL-data are similar to their counterparts obtained using BOLD-data-alone, but most of the significant connections estimated from ASL-data were stronger. This is largely a result of increased identifiability of the model, due to the additional information provided in the CBF data; i.e. the uncertainty about the connectivity estimated is reduced (as indicated above by the increase in KL divergence). Heuristically, the more precise data afforded by ASL 'pulls' the posterior estimates further from their prior means. Note that, as a consequence, large connections became more pronounced, while many of the weaker connections shrinked towards their prior mean of zero. We verified this behavior by performing simulations to reproduce the increased connectivity strengths of the strongest connections (see Supplementary material 2). The correlation between connectivity estimates based on BOLD-data-alone and ASL-data was the lowest for 2S-DCM (r~0.85), slightly higher for S-DCM (r~0.90) and the highest for P-DCM (r~0.96). As CBF is more closely related to neuronal activity, it is reasonable to assume that ASL data – with sufficient SNR – provides a more accurate connectivity estimate than BOLD-data-alone. Nevertheless, the high correlation of the connectivity patterns using both data sets suggests that BOLD-data-alone provides reasonably accurate estimates of connectivity, even without additional information in CBF data (but see below). The stability of the connectivity estimates is the highest for P-DCM, arguing for the physiologically informed assumptions embedded with P-DCM. Moreover, there is not only a good agreement between estimated connectivity from these two modalities, but also between local (within-subject) parameter estimates of the generative model such as: inhibitory-excitatory connections μ; inhibitory gain factors λ; global self-inhibition σ; mean transit times t_{MTT}; and viscoelastic constants τ (results not shown). In addition, the decay parameter χ controlling the NVC in ASL data diverged negligibly from its prior mean (see the Supplementary material 1 for parameter description).

We showed that in comparison to BOLD-data-alone, all models fitted to ASL-data scored higher PVE values. For BOLD responses, the PVE values were on average ~2% higher (see Table 3 and Fig. 7). Interestingly, in the case of S-DCM and 2S-DCM, the PVE values for CBF responses were even higher than for BOLD responses. One explanation of this result could be that the size of post-stimulus CBF deactivation is smaller than the post-stimulus BOLD undershoot (as generally observed). This means that neuronal and NVC mechanisms as implemented in S-DCM and 2S-DCM can explain this size of post-stimulus CBF deactivation; however, they are insufficient to explain the even larger post-stimulus BOLD undershoot. This is because S-DCM and 2S-DCM assume coupled dynamics between CBF and CBV, which can only result in a post-stimulus BOLD undershoot that is smaller or comparable to the post-stimulus deactivation in the CBF response

(Havlicek et al., 2015). Unlike S-DCM and 2S-DCM, P-DCM explains the discrepancy between post-stimulus deactivation in the CBF and post-stimulus undershoot in the BOLD response by CBF-CBV uncoupling; i.e. BOLD response can have more pronounced post-stimulus undershoot than CBF (Havlicek et al., 2015). This result points to the importance of CBF-CBV uncoupling as a component of the generative model, and that the generative models of S-DCM and 2S-DCM are not well suited for modeling of ASL data, where it is necessary to account for differences in dynamic behavior of CBF and BOLD responses. Moreover, P-DCM scored the highest PVE values for CBF responses, i.e. providing the most accurate predictions of the CBF response shape (including the post-stimulus deactivation) in all brain regions. This was achieved by modeling regional E-I balance together with the connectivity between regions. Since P-DCM did not estimate negative feedback connections as in S-DCM, the origin of post-stimulus deactivations in CBF responses can be traced directly to the inhibitory activity (i.e. causing a reduction of excitatory activity below baseline), which is in agreement with (e.g. (Mullinger et al., 2013; Sadaghiani et al., 2009; Shmuel et al., 2006)).

Finally, it is worth mentioning that there are some interesting differences in connectivity estimates as provided by P-DCM compared to other models (see Fig. 4). In particular, in P-DCM connectivity results based on ASL-data, we see negative contralateral connections between left and right M1s. These small negative weights are in good agreement with our observations that most of the subjects showed small ipsilateral deactivation in M1 during finger tapping. Moreover, these ipsilateral deactivations in M1 and in sensory areas are regularly observed (e.g. see (Hlushchuk and Hari, 2006; Klingner et al., 2011a; Klingner et al., 2011b; Mullinger et al., 2014; Stefanovic et al., 2004)). Furthermore, P-DCM does not show any significant connections between right and left V1s (in both ASL-data and BOLD-data-alone), but there are stronger cross-hemispheric connections estimated by S-DCM and 2S-DCM. Given the fact that we tried to minimize possibility of contralateral activation of V1 by experimentally controlling background iso-luminance with respect to checkerboard stimuli, and we did not observe any significant activations and deactivations in hemodynamic responses on ipsilateral sides of the visual cortex, we can quite safely assume that these connections detected by S-DCM and 2S-DCM are spurious. Therefore, by considering this specific experimental manipulation, P-DCM (especially with ASL-data) provides more sensible connectivity estimate with better reflection of the underlying physiological processes. In short, the construct validity of P-DCM, with respect to known functional anatomy and our assumptions about connectivity architecture is reasonable.

Generalizability and limitations

We used experimental data from a visuo-motor paradigm and five significantly activated brain regions. Theoretically, this task – and the number of regions – allow for testing many competing hypothesis about connectivity structures and their induced changes. Although our experimental task has a fully factorial design, where we could test for the main effect of switch (ipsilateral vs. contralateral conditions) and interaction between switch and response side (right vs. left), we only considered connectivity changes between ipsilateral and contralateral conditions. This can be motivated by noting that the interactions between switch and response side can be modeled implicitly, through the bilinear effects in our DCM. This choice of functional architecture (see Fig. 3) was motivated by an initial BMS analysis, which showed that a model with fully factorial condition-specific effects on connectivity had less evidence than the simpler architecture used in the paper (results not shown).

Moreover, weights modulating transcallosal connections between left and right V1 were excluded from the models, even though one might think that these connections play an important role in propagating neuronal activity during contralateral conditions (e.g. communicat-

ing activity from left V1 to right M1 via right V1). However, also this hypothesis was not supported by our data and was rejected during the initial BMS (largely because there was no significant increase in the BOLD response of the opposite V1, see Fig. 6). In short, the connectivity structure used in this paper was selected based on BMS. Importantly, this model was strongly preferred by all DCM variants (S-DCM, 2S-DCM, and P-DCM). It is unlikely that alternative (but plausible) connectivity architectures would result in fundamentally different conclusions with respect to the physiological components in P-DCM. This is due to the fact that fMRI transients, as observed in this study, cannot be fully accounted for by S-DCM and 2S-DCM neither locally (see Havlicek et al. (2015)) or remotely, via interaction with other brain regions. This is reflected by the large differences in log-evidences for the DCM variants we considered (but see below).

It should be emphasized that the primary goal of this paper was not to identify the best structural connectivity model for the task, but rather to evaluate relevant components of neuronal and hemodynamic models and their impact on connectivity estimates. That is, the experimental data furnish transients observed in typical fMRI data and how these transients affect connectivity estimates under different DCM variants. However, the superiority of P-DCM, relative to S- and 2S-DCM, may not generalize to all experimental designs and functional activation patterns. For example, we used a block design with resting durations that were sufficiently long to allow for the full evolution of the post-stimulus BOLD undershoot. It might be that if other experimental designs are used (e.g. fast event-related design, where the post-stimulus undershoot cannot be easily detected) or if no regional response contains a post-stimulus undershoot and/or exhibits adaptation during stimulation, Bayesian model comparison may lead to different conclusions. However, as undershoot and adaptation are commonly observed features of the fMRI signal and the ability of P-DCM to effectively model these physiological processes, our conclusions may hold for the majority of fMRI studies. Finally, note that even in those cases for which S- and 2S-DCM are superior, it is expected that the connectivity patterns obtained with P-DCM are similar to those with S- and 2S-DCM.

We compared DCM models using BOLD-data-alone and ASL-data, and showed that the CBF part of ASL-data can improve the model inversion (see above). However, since the estimated neuronal signal can be contaminated by vascular dynamics that were not sufficiently explained by the hemodynamic model (as shown for S- and 2S-DCM), one may wonder if inverting the model directly from CBF time-courses (derived from ASL data using surround subtraction) would be a better choice. This means that one would connect the neuronal model only with NVC to generate CBF responses and fit these to the data. We have also tested this model in the early phase of our DCM analysis, and found it to resemble results observed using BOLD-data-alone and ASL-data. However, due to low SNR of CBF, the variability in estimated parameters was significantly higher (results not shown). This also suggests that both CBF and BOLD data provide physiological constraints to the model being inverted.

BOLD-data-alone was derived from the ASL-data using surround averaging, which results in a smoother BOLD signal, compared to when BOLD data is acquired separately. Theoretically, this smoothing can remove some neuronal or vascular information from the data, which could then decrease the efficiency of model inversion. Therefore, to minimize possible effects of smoothing on model inversion, we included a temporal smoothing of BOLD signals by the equivalent kernel (see Methods and Supplementary material 1). In addition, simulation results indicated that, if the smoothing is taken into account, the difference between using BOLD signal derived from ASL data and BOLD signal acquired separately is minimal (see Supplementary material 2).

The new ASL-DCM model assumes that ASL data are acquired at a single TE. We used TE=17 ms to ensure a good signal quality trade-off between CBF and BOLD signals, which means that both CBF and

BOLD signals have slightly suboptimal SNR properties. By saying that, in principle one could benefit from an improved SNR of both CBF and BOLD data by using a multi-TE sequence (Poser et al., 2006; Simon et al., 2013; Woolrich et al., 2006). For example, for a dual-echo sequence, the first TE can be optimized for CBF (e.g. 8 ms) and the second for the BOLD signal (e.g. 35 ms). Additionally, further improvements in CBF SNR could be achieved by filtering out the physiological noise associated with cardiac and respiratory fluctuations (e.g. (Restom et al., 2006)) or by reducing noise from the static tissue compartment by using ASL sequence with background suppression (e.g. (Ghariq et al., 2014)). However, if background suppression is used, the BOLD signal equation has to be adjusted due to altered contribution of the extravascular and intravascular signals (Uludağ et al., 2009). Finally, our modeling approach leads to denosing of CBF signal as well. It was argued earlier (Simon et al., 2013; Woolrich et al., 2006) and confirmed by our results of improved connectivity and hemodynamic response estimates that dynamic estimates of CBF signal can be partly denoised by combining information from simultaneously acquired CBF and BOLD data by physiologically constrained modeling – especially if a physiologically informed model such as P-DCM is used.

Theoretically, as the ASL signal is acquired with a nonzero TE, BOLD weighting contaminates CBF signal. In general, there are two sources of BOLD contamination of the CBF signal (Liu and Wong, 2005): (1) A spurious BOLD component contaminates CBF signal derived from ASL data if only a basic control-tagged subtraction is used. However, this source of contamination can be reduced if subtraction approaches combined with surround averaging are employed (Lu et al., 2006) or avoided if direct modeling of the ASL signal is applied (Mumford et al., 2006). (2) Intrinsic BOLD weighting of the CBF signal is always present and can be modeled by assuming a multiplicative modulation of CBF signal by the BOLD component (Liu and Wong, 2005; Lu et al., 2006; Woolrich et al., 2006). This source of BOLD contamination can be partly reduced by choosing a lower TE. However, for functional studies that focus on analysis of induced responses normalized to baseline values in cortical areas, this contamination is very small for the MRI parameters utilized in this study (i.e. $B_0=3$ T and TE=17 ms). Therefore, we have not included this BOLD contamination effect in our model of the ASL signal. Note, however, this effect may become more significant at higher TE values and/or magnetic field strengths.

Summary

Using experimental fMRI data, we found that P-DCM is statistically superior to S-DCM and 2S-DCM for evaluating effective connectivity among distributed ROIs. This was demonstrated by fitting these models to both BOLD-data-alone and combined BOLD-CBF-data via an extended DCM for ASL data. Our results indicate that P-DCM is the most consistent among all three models, in terms of the agreement between connectivity estimates, and had the lowest inter-subject variability. Nevertheless, connectivity differences between conditions are also well characterized by S-DCM. These results speak in favor of using P-DCM in the standard DCM for fMRI effective connectivity analysis performed on BOLD data. Overall, the statistical superiority of P-DCM over S-DCM and 2S-DCM suggests the importance of accurately modeling physiological mechanisms to deduce the neuronal connectivity from indirect fMRI data. These results, thus, confirm our earlier premise that P-DCM is a physiologically plausible model of fMRI data.

In addition, we argue that P-DCM has the potential to provide better estimates of effective connectivity and is less dependent on vascular sources of hemodynamic response variability, compared to S- and 2S-DCM. The validity of P-DCM is further strengthened if ASL data is used, since it provides direct access to CBF, a crucial variable that helps identifying vascular transients in hemodynamic responses. Finally, we could speculate that the ability of P-DCM to model neuronal

transients due to neuronal inhibition/adaptation that are reflected in observed hemodynamic responses (in addition to the vascular transients) could provide a unique opportunity to study changes in effective connectivity driven by neuronal inhibition.

Appendix A. Supporting information

Supplementary data associated with this article can be found in the online version at doi:10.1016/j.neuroimage.2017.03.017.

References

Agosta, F., Rocca, M.A., Pagani, E., Absinta, M., Magnani, G., Marcone, A., Falautano, M., Comi, G., Gorno-Tempini, M.L., Filippi, M., 2010. Sensorimotor network rewiring in mild cognitive impairment and Alzheimer's disease. Hum. Brain Mapp. 31, 515–525.

Buxton, R.B., Wong, E.C., Frank, L.R., 1998. Dynamics of blood flow and oxygenation changes during brain activation: the balloon model. Magn. Reson. Med. 39, 855–864.

Chen, J.J., Pike, G.B., 2009. Origins of the BOLD post-stimulus undershoot. NeuroImage 46, 559–568.

Crossley, N.A., Mechelli, A., Fusar-Poli, P., Broome, M.R., Matthiasson, P., Johns, L.C., Bramon, E., Valmaggia, L., Williams, S.C.R., McGuire, P.K., 2009. Superior temporal lobe dysfunction and frontotemporal dysconnectivity in subjects at risk of psychosis and in first-episode psychosis. Hum. Brain Mapp. 30, 4129–4137.

David, O., Kiebel, S.J., Harrison, L.M., Mattout, J., Kilner, J.M., Friston, K.J., 2006. Dynamic causal modeling of evoked responses in EEG and MEG. NeuroImage 30, 1255–1272.

Donahue, M.J., Faraco, C.C., Strother, M.K., Chappell, Ma, Rane, S., Dethrage, L.M., Hendrikse, J., Siero, J.C.W., 2014. Bolus arrival time and cerebral blood flow responses to hypercarbia. J. Cereb. 34, 1243–1252.

Friston, K., 2011. Functional and effective connectivity: a review. Brain Connect. 1, 13–36.

Friston, K., Daunizeau, J., Stephan, K.E., 2013. Model selection and gobbledygook: response to Lohmann et al. NeuroImage 75, 275–278.

Friston, K., Mattout, J., Trujillo-Barreto, N., Ashburner, J., Penny, W., 2007. Variational free energy and the Laplace approximation. NeuroImage 34, 220–234.

Friston, K.J., 1994. Functional and effective connectivity in neuroimaging: a synthesis. Hum. Brain Mapp. 2, 56–78.

Friston, K.J., Harrison, L., Penny, W., 2003. Dynamic causal modelling. NeuroImage 19, 1273–1302.

Friston, K.J., Holmes, aP., Worsley, K.J., Poline, J.P., Frith, C.D., Frackowiak, R.S.J., 1995. Statistical parametric maps in functional imaging: a general linear approach. Hum. Brain Mapp. 2, 189–210.

Friston, K.J., Kahan, J., Biswal, B., Razi, A., 2014. A DCM for resting state fMRI. NeuroImage 94, 396–407.

Friston, K.J., Penny, W.D., Glaser, D.E., 2005. Conjunction revisited. NeuroImage 25, 661–667.

Ghariq, E., Chappell, M.A., Schmid, S., Teeuwisse, W.M., Osch, M.J.P.V., 2014. NeuroImage Effects of background suppression on the sensitivity of dual-echo arterial spin labeling MRI for BOLD and CBF signal changes. NeuroImage 103, 316–322.

Gonzalez-Castillo, J., Saad, Z.S., Handwerker, D., Inati, S.J., Brenowitz, N. Bandettini, P., 2012. Whole-brain, time-locked activation with simple tasks revealed using massive averaging and model-free analysis. Proc. Natl. Acad. Sci. USA 109, 5487–5492.

Handwerker, D.A., Ollinger, J.M., D'Esposito, M., 2004. Variation of BOLD hemodynamic responses across subjects and brain regions and their effects on statistical analyses. NeuroImage 21, 1639–1651.

Havlicek, M., Ivanov, D., Poser, B.A., Uludag, K., 2017. Echo-time dependence of the BOLD response transients – a window into brain functional physiology. Submitted for publication.

Havlicek, M., Roebroeck, A., Friston, K., Gardumi, A., Ivanov, D., Uludak, K., 2015. Physiologically informed dynamic causal modeling of fMRI data. NeuroImage 122, 355–372.

Hernandez-Garcia, L., Jahanian, H., Rowe, D.B., 2010. Quantitative analysis of arterial spin labeling fMRI data using a general linear model. Magn. Reson. Imaging 28, 919–927.

Hluschchuk, Y., Hari, R., 2006. Transient suppression of ipsilateral primary somatosensory cortex during tactile finger stimulation. J. Neurosci. 26, 5819–5824.

Hoge, R.D., Atkinson, J., Gill, B., Crelier, G.R., Marrett, S., Pike, G.B., 1999. Stimulus-dependent BOLD and perfusion dynamics in human V1. NeuroImage 9, 573–585.

Huber, L., Ivanov, D., Krieger, S.N., Streicher, M.N., Mildner, T., Poser, Ba, Möller, H.E., Turner, R., 2014. Slab-selective, BOLD-corrected VASO at 7 Tesla provides measures of cerebral blood volume reactivity with high signal-to-noise ratio. Magn. Reson. Med. 72, 137–148.

Kass, R.E., Raftery, A.E., 1995. Bayes factors. J. Am. Stat. Assoc. 90, 773–795.

Klingner, C.M., Ebenau, K., Hasler, C., Brodoehl, S., Görlich, Y., Witte, O.W., 2011a. Influences of negative BOLD responses on positive BOLD responses. NeuroImage 55, 1709–1715.

Klingner, C.M., Huonker, R., Flemming, S., Hasler, C., Brodoehl, S., Preul, C., Burmeister, H., Kastrup, A., Witte, O.W., 2011b. Functional deactivations: multiple ipsilateral brain areas engaged in the processing of somatosensory information. Hum. Brain Mapp. 32, 127–140.

Liu, T.T., Brown, G.G., 2007. Measurement of cerebral perfusion with arterial spin labeling: part 1. Methods, 517–525.

Liu, T.T., Wong, E.C., 2005. A signal processing model for arterial spin labeling functional MRI. NeuroImage 24, 207–215.

Logothetis, N.K., Wandell, Ba, 2004. Interpreting the BOLD signal. Annu. Rev. Physiol. 66, 735–769.

Lu, H., Donahue, M.J., Zijl, P.C.M.V., 2006. Detrimental Effects of BOLD Signal in Arterial Spin Labeling fMRI at High Field Strength. 552, 546–552.

Lu, H., Golay, X., Pekar, J.J., Van Zijl, P.C.M., 2003. Functional magnetic resonance imaging based on changes in vascular space occupancy. Magn. Reson. Med. 50, 263–274.

Mandeville, J.B., Marota, J.J.A., Ayata, C., Zaharchuk, G., Moskowitz, M.A., Rosen, B.R., Weisskoff, R.M., 1999. Evidence of a cerebrovascular postarteriole windkessel with delayed compliance. J. Cereb. Blood Flow. Metab. 19, 679–689.

Marreiros, A.C., Kiebel, S.J., Friston, K.J., 2008. Dynamic causal modelling for fMRI: a two-state model. NeuroImage 39, 269–278.

Miyake, Y., Okamoto, Y., Onoda, K., Shirao, N., Okamoto, Y., Otagaki, Y., Yamawaki, S., 2010. Neural processing of negative word stimuli concerning body image in patients with eating disorders: an fMRI study. NeuroImage 50, 1333–1339.

Mullinger, K.J., Mayhew, S.D., Bagshaw, A.P, Bowtell, R., Francis, S.T., 2013. oststimulus undershoots in cerebral blood flow and BOLD fMRI responses are modulated by poststimulus neuronal activity. Natl. Acad. Sci. 13, 13636–13641.

Mullinger, K.J., Mayhew, S.D., Bagshaw, A.P., Bowtell, R., Francis, S.T., 2014. Evidence that the negative BOLD response is neuronal in origin: a simultaneous EEG-BOLD-CBF study in humans. NeuroImage 94, 263–274.

Mumford, J.A., Hernandez-Garcia, L., Lee, G.R., Nichols, T.E., 2006. Estimation efficiency and statistical power in arterial spin labeling fMRI. NeuroImage 33, 103–114.

Penny, W.D., 2012. Comparing dynamic causal models using AIC, BIC and free energy. NeuroImage 59, 319–330.

Penny, W.D., Stephan, K.E., Daunizeau, J., Rosa, M.J., Friston, K.J., Schofield, T.M., Leff, A.P., 2010. Comparing families of dynamic causal models. PLoS Comput. Biol. 6, (e1000709-e1000709).

Poser, B.A., Versluis, M.J., Hoogduin, J.M., Norris, D.G., 2006. BOLD contrast sensitivity enhancement and artifact reduction with multiecho EPI: parallel-acquired inhomogeneity-desensitized fMRI. Magn. Reson. Med. 55, 1227–1235.

Renvall V., Nangini C., Hari R., All that glitters is not BOLD: inconsistencies in functional MRI,Scientific Reports 4, 2014, 3920 (1-3).

Restom, K., Behzadi, Y., Liu, T.T., 2006. Physiological noise reduction for arterial spin labeling functional MRI. NeuroImage 31, 1104–1115.

Rocca, M.A., Pagani, E., Absinta, M., Valsasina, P., Falini, A., Scotti, G., Comi, G., Filippi, M., 2007. Altered functional and structural connectivities in patients with MS: a 3-T study. Neurology 69, 2136–2145.

Roebroeck, A., Formisano, E., Goebel, R., 2011. The identification of interacting networks in the brain using fMRI: model selection, causality and deconvolution. NeuroImage 58, 296–302.

Rosa, M.J., Kilner, J.M., Penny, W.D., 2011. Bayesian comparison of neurovascular coupling models using EEG-fMRI. PLoS Comput. Biol. 7, (e1002070-e1002070).

Sadaghiani, S., Uğurbil, K., Uludağ, K., 2009. Neural activity-induced modulation of BOLD poststimulus undershoot independent of the positive signal. Magn. Reson. Imaging 27, 1030–1038.

Seghier, M.L, Zeidman, P., Neufeld, N.H., Leff, A.P., Price, C.J., 2010. Identifying abnormal connectivity in patients using Dynamic Causal Modelling of fMRI responses. Front. Syst. Neurosci. 4, 1–14.

Shmuel, A., Augath, M., Oeltermann, A., Logothetis, N.K., 2006. Negative functional MRI response correlates with decreases in neuronal activity in monkey visual area V1. Nat. Neurosci. 9, 569–577.

Shmuel, A., Yacoub, E., Pfeuffer, J., Van de Moortele, P.F., Adriany, G., Hu, X., Ugurbil, K., 2002. Sustained negative BOLD, blood flow and oxygen consumption response and its coupling to the positive response in the human brain. Neuron 36, 1195–1210.

Simon, A.B., Griffeth, V.E.M., Wong, E.C., Buxton, R.B., 2013. A novel method of combining blood oxygenation and blood flow sensitive magnetic resonance imaging techniques to measure the cerebral blood flow and oxygen metabolism responses to an unknown neural stimulus. PLoS One 8, (e54816-e54816).

Stefanovic, B., Warnking, J.M., Pike, G.B., 2004. Hemodynamic and metabolic responses to neuronal inhibition. NeuroImage 22, 771–778.

Stephan, K.E., Kasper, L., Harrison, L.M., Daunizeau, J., den Ouden, H.E.M., Breakspear, M., Friston, K.J., 2008. Nonlinear dynamic causal models for fMRI. NeuroImage 42, 649–662.

Stephan, K.E., Penny, W.D., Moran, R.J., den Ouden, H.E.M., Daunizeau, J., Friston, K.J., 2010. Ten simple rules for dynamic causal modeling. NeuroImage 49, 3099–3109.

Stephan, K.E., Weiskopf, N., Drysdale, P.M., Robinson, P.A., Friston, K.J., 2007. Comparing hemodynamic models with DCM. NeuroImage 38, 387–401.

Tak, S., Kempny, A.M., Friston, K.J., Leff, A.P., Penny, W.D., 2015. Dynamic causal modelling for functional near-infrared spectroscopy. NeuroImage 111, 338–349.

Uludağ, K., Müller-Bierl, B., Uğurbil, K., 2009. An integrative model for neuronal activity-induced signal changes for gradient and spin echo functional imaging. NeuroImage 48, 150–165.

Valdes-Sosa, P.A., Roebroeck, A., Daunizeau, J., Friston, K., 2011. Effective connectivity: influence, causality and biophysical modeling. NeuroImage 58, 339–361.

Valdes Sosa, P.A., Sanchez Bornot, J.M., Sotero, R.C., Iturria Medina, Y., Aleman Gomez, Y., Bosch Bayard, J., Carbonell, F., Ozaki, T., 2009. Model driven EEG/fMRI fusion of brain oscillations. Hum. Brain Mapp. 30, 2701–2721.

Wong, E.C., Buxton, R.B., Frank, L.R., 1997. Implementation of quantitative perfusion imaging techniques for functional brain mapping using pulsed arterial spin labeling. NMR Biomed. 10, 237–249.

Woolrich, M.W., Chiarelli, P., Gallichan, D., Perthen, J., Liu, T.T., 2006. Bayesian inference of hemodynamic changes in functional arterial spin labeling data. Magn. Reson. Med. 56, 891–906.